Laboratory measurements and computer simulations of highly curved flow after sluice gate

Bowen Xu

A Thesis

in

The Department

of

Building, Civil, and Environmental Engineering

Presented in Partial Fulfilment of the Requirements

For the Degree of Master of Applied Science in Civil Engineering at

Concordia University

Montreal, Quebec, Canada

June 2018

CONCORDIA UNIVERSITY

School of Graduate Studies

This is to certify that the thesis prepared

By: Bowen Xu

Entitled: Laboratory Measurements and Computer Simulations of Highly Curved Flow after Sluice Gate

and submitted in partial fulfillment of the requirements for the degree of

Master of Applied Science (Civil Engineering)

complies with the regulations of the University and meets the accepted standards with respect to originality and quality.

Signed by the final Examining Committee:

Dr. C. Mulligan Chair

Chair's name

Dr. M. Paraschivoiu Examiner

Examiner's name

Dr. A. Nazemi Examiner

Examiner's name

Dr. S. Li Supervisor

Supervisor's name

Approved by _____

Chair of Department or Graduate Program Director

_____ 2018 _____

Dean of Faculty

ABSTRACT

Laboratory Measurements and Computer Simulations of

Highly Curved Flow after Sluice Gate

Bowen Xu

Sluice-gates are widely used for such purposes as the control of discharges and water levels in hydraulic engineering systems. It is important to understand the features of turbulent flow passing underneath a sluice-gate. Previously, a great deal of research attention has centred on such flow features as the head-discharge relationship and the pressure distribution over the gate surfaces, leading to impressive progress in those aspects of the turbulent flow problem. However, little attention has been paid to the curvature of flow profiles immediately downstream of the gate. This is in spite of its relevance to the optimal design and safe operations of sluice-gates.

The purpose of this research work is to characterise the highly curved turbulent flow through laboratory flume experiments and to extend the experimental results by computer simulations. The experiments covered the conditions that the gate opening ranged from one to two inches and the ratio of the upstream depth to the gate opening ranged from four to 16. The computer simulations produced finite volume solutions to the Reynolds-averaged Navier-Stokes equations. Under the same conditions as the flume experiments, the computed flow profiles as well as pressure distributions from the simulations compare well with the experimental data. Much of the success in computations is attributable to the implementation of rigorous procedures to validate mesh convergence, the independence of numerical results on time step and initial conditions used, and the suitability of turbulence closure schemes. The shear stress transport k-ω model is shown to be a suitable model for turbulence closure. It is shown that the volume of fluid method works well for tracking the highly curved free water surface.

This thesis reports further computational results of the flow and pressure fields for large gate openings up to 16 inches, which are close to field scales or prototype scales, and which are difficult and expensive to set up in laboratories. Using the new experimental and computational results, reliable relationships for flow curvature parameters, including the radius of the circle of curvature, the centre of the circle, and the angle of a tangent to the free surface with the channel-bottom, have been developed. The introduction of these new relationships to the permanent literature about sluice-gate flows represents a significant contribution from this research work. This thesis also provides an update of the contraction distance and coefficient, the results being consistent with the literature values. Moreover, corrections to some existing formulations of the sluice-gate flow problem are proposed.

Acknowledgements

It is my great honour to be a MSc student of Dr. Samuel Li. I have acquired the solid knowledge and experience throughout his guidance, encouragement and support throughout the study and research. For the presentation of this thesis, his abundant help, guidance and support are especially appreciated. Dr. Li is a truly excellent supervisor to me.

Besides my supervisor, I also would like to express my appreciations to the rest of my committee members: Drs. Catherine Mulligan, Marius Paraschivoiu, Ali Nazemi for their insightful comments and suggestions.

I would like to thank my dear parents, Zhijian Xu and Li Xu, for their tremendous help and support through the whole duration of my studies.

I also would like to express my thanks to my friends and colleagues. With their help and support, I have avoided many detours during my study and research.

Finally, this study received financial support from the Natural Science and Engineering Research Council of Canada and Concordia University.

List of Contents

List of Symbols

The following symbols have been used in this thesis:

English Letters

A	Cross section area (m^2);
b	Width of the flume channel (m);
C_c	Contraction coefficient;
C_1	standard k-ε model adjustable constant;
C_2	standard k-ε model adjustable constant;
C_μ	standard k-ε model adjustable constant;
Co	Courant number;
$D_{k\omega}$	Cross-diffusion term;
C_d	Discharge coefficient;
F	Froude number;
F_1	Blending function for SST k-ω model;
F_2	Blending function for SST k-ω model;
g	Gravitational acceleration (m/s^2);
H_p	Dimensionless bottom pressure head;
h_p	Bottom pressure head (Pa);
h_U	Bottom pressure head at upstream where x_1/w = -5 (Pa);
h_D	Bottom pressure head at downstream where x_1/w = 5 (Pa);
k	Turbulence kinetic energy (m^2/s^2);
L	Reference length (m);
P_i	Pressure of location i (Pa);

p	Reynolds-averaged pressure (Pa);
Q	Flow discharge (m^3/s);
Re_x	Local Reynolds number;
$Re_{x\,crit}$	Critical Reynold number;
r	Radius of the circle of curvature (m);
T	Simulation time period (s);
t	Time (s);
u_γ	Surface Internal energy density (m^2kg/s^2);
u_i	Flow velocity in the x_i-direction (m/s);
u_{1m}	cross-sectionally averaged velocity (m/s);
u_i'	Velocity fluctuation in the x_i-direction (m/s);
u_0	freestream velocity (m/s);
w	Sluice-gate opening (m);
x_c	Contraction distance (m);
x_o	Coordinate of a point in the x_i-direction;
y_1	Depth of the approach flow upstream of a sluice gate (m);
y_2	Flow depth at the vena contracta (m);

Greek Letters

α	Energy coefficient;
α_w	Volume fraction of water;
α_1	SST k-ω model adjustable constant;
α_2	SST k-ω model adjustable constant;
β	Momentum coefficient;
β_1	SST k-ω model adjustable constant;
β_2	SST k-ω model adjustable constant;
β^*	SST k-ω model adjustable constant;
δ	Boundary layer thickness;
δ_{ij}	Kronecker delta;
δx	Mesh size in the numerical model;
ε	Rate of dissipation of turbulence energy (m^2/s^3);
κ	Curvature (m^{-1});
μ_a	Dynamic viscosity of air ($N{\cdot}s/m^2$);
μ_w	Dynamic viscosity of water ($N{\cdot}s/m^2$);
μ_t	Turbulent eddy viscosity;
μ	Dynamic viscosity of a mixture of air and water ($N{\cdot}s/m^2$);
ρ	Density of a mixture of air and water (kg/m^3);
ρ_a	Density of air (kg/m^3);
ρ_w	Density of water (kg/m^3);
σ_k	Standard k-ε model adjustable constant;
σ_ε	Standard k-ε model adjustable constant;

σ_{k1}	SST k-ω model adjustable constant;
σ_{k2}	SST k-ω model adjustable constant;
$\sigma_{\omega 1}$	SST k-ω model adjustable constant;
$\sigma_{\omega 2}$	SST k-ω model adjustable constant;
τ_{ij}	Turbulent stress (N/m^2);
τ_{ω}	Wall shear stress (N/m^2);
v	Kinematic viscosity of a fluid (m^2/s);
ν_T	Kinematic eddy viscosity (m^2/s);
ω	specific rate of dissipation of the turbulence kinetic energy k into internal thermal energy (s^{-1});

Abbreviation

CFD	Computational Fluid Dynamics;
FVM	Finite volume method;
RANS	Reynolds-averaged Navier-Stokes;
SST	Shear stress transport;
VOF	Volume of fluid;

List of Figures

List of Tables

Chapter One Introduction

1.1 Background

Sluice-gates have commonly been used to control discharge and water level in the water and wastewater industry. When a water channel is controlled by a gate at its head, the channel is called as a sluice. In the domain of water and wastewater control, the terms, such as slide gate, knife gate, sluice gate and sluice, are used interchangeably. Traditionally, sluice gates are built using either wooden or metal materials.

First, sluice gates were used to allow excessive water to flow over an overflow-spillway. Examples include the investigation of water level drop in Lake Victoria, Nairobi, Kenya by Kull (2006), in connection with the Kiira Dam built close to the lake. The author suggested that the sluice gate provided a direct control of the flowrate to ensure the safety of the dam operations. Other examples include the use of sluice gates to determine the amount of water passing through turbines for electricity productions.

In other cases, sluice gates have been used to provide a mechanism for achieving desirable flowrates in power and irrigation canals, wastewater transport and treatment streams, and water supply facilities. For instance, Lozano et al. (2009) performed field calibrations of submerged sluice gates in irrigation canals. Their field work dealt with an irrigation canal in Lebrija, Spain. This canal connected four pools. Four sluice gates were installed in the canal, with sensors for tracking water levels and discharges, and for providing desirable flowrates in the canal by adjusting the gate opening.

Besides the typical applications discussed above, sluice gates have been used to regulate the water discharge and water level in order to make efficient use of the lake water (Zhang et al. 2003). There are cases of using sluice gates in natural rivers as well as man-made waterways for

such purposes as flood defences and mitigations, shipping, and floating debris control (Baek et al. 2015; Wang et al. 2016).

The flow of water passing underneath a sluice gate is an important topic in hydraulic engineering. In the past a few decades, many researchers have used different approaches to investigate the characteristics of sluice gate flows. Masliyah et al. (1985) introduced boundary-fitted coordinates methods for accurate evaluations of the discharge coefficient and for predictions of free-surface profiles on upstream and downstream sides of a sluice gate. Finnie et al. (1991) used a finite element computer code to calculate the velocities upstream of a sluice gate and pressure distribution on the upstream face of the sluice gate They also studied the kinetic energy and its dissipation rate around the sluice gate.

Montes (1997) proposed mathematical methods to evaluate water surface profiles, velocity, and pressure distribution around a sluice gate. Shammaa et al. (2005) studied the velocity field upstream of a sluice gate and orifice. On the basis of momentum conservation, Belaud et al. (2009) studied the contraction coefficient under sluice gates for both free and submerged flows. Habibzadeh et al. (2011) proposed a theory for the calculation of the discharge coefficient under both free and submerged flow conditions. They introduced an energy-loss factor to improve the results of hydraulic energy loss. Regarding the flow characteristics upstream and downstream of a sluice gate, Cassan and Belaud (2012) investigated the energy and momentum coefficients, head loss, friction forces, and contraction coefficient by using numerical models.

In recent years, researchers have used sluice gates in their studies of many flow phenomena, including the hydraulic jump (Zhang et al. 2014; Chern and Syamsuri 2013), water flow behaviors (Xie amd Lim 2015; Termini 2009; Zimmer et al. 2013), and sediment transport (Zhang et al. 2013; Moreno et al. 2016). However, neither the issue of flow curvatures between

the gate opening and the section of vena contracta, nor the issue of resultant forces on the sluice gate has been addressed in the previous studies.

1.2 Objectives of this research

It is clear that sluice gates are important hydraulic structures. Previously, researchers have used experimental and numerical methods to investigate the characteristics of sluice gate flows. The flow of water on the downstream side of the gate in question can be free flow or submerged flow. So far, researchers of the sluice gate flow problem have focused on the contraction coefficient, C_c, discharge coefficient, C_d, and their dependence on the ratio of the upstream flow depth to the sluice gate opening, y_1/w.

The existing studies have made little efforts to investigate the curvature distributed along the free water surface downstream of the sluice gate. The issue of flow curvature is important. Thus, there is a gap of knowledge, which has motivated this thesis study. This study aims is to provide a detailed description of the curvature distribution.

The sub-objectives of this study are: 1) to understand the characteristic of highly curved flows passing underneath a sluice-gate through flume experiments; and 2) to extend the experimental results by computer simulations. The dual approach of physical experiments and numerical simulations would be effective to achieve an improved understanding of the flow curvature. This is of engineering relevance to the optimal design and safe operations of sluice-gates.

1.3 Scope of the research work

The contents of this thesis are organised into six chapters. In the following, Chapter Two presents a review of the pertinent literature, and explains the motivation of this research work. The literature review covers studies using experimental and numerical methods.

Then, Chapter Three describes the laboratory experiments conducted in the Water Resources Engineering Laboratory at Concordia University. The description includes the experimental setup, flow conditions, and measurements methods. The experiments provide the first-hand data for validations of the numerical model. The validations are accomplished by comparing water flow profiles and pressure distributions on the gate surfaces between the experiments and numerical computations.

Next, Chapter Four provides detailed explanations of the numerical simulations, which include:

- The Computational Fluid Dynamics (CFD) method implemented in the numerical simulations;
- OpenFOAM, an open-source CFD software, used as a tool for the development of numerical solvers. The solvers are based on the Finite Volume Method (FVM);
- The continuity equation and momentum equations of motion;
- The Reynolds-averaged Navier-Stokes equations;
- The volume of fluid (VOF) method for tracking the interface of two-phase flow.

Subsequently, Chapter Five discusses the experimental and numerical results, along with data comparisons. The results include:

- water flow profiles;
- the contraction distance and coefficient;

- pressure distributions on the sluice gate surfaces and the channel-bottom;
- the curvature of the rapidly varied flow surface downstream of the sluice gate;
- boundary layer thickness;
- velocity vectors and kinetic energy distributions close to the sluice gate;
- evaluation of some assumptions made in earlier studies;
- the performance of the standard k-ε and SST k-ω models.

Finally, Chapter Six provides highlights of the conclusions from this research work.

1.4 Main contributions from this research work

The main contributions from this research work are highlighted below:

- A knowledge gap about turbulent underflow in the vicinity of a sluice-gate has been filled through the research work reported in this thesis;
- For the first time, useful relationships for some key flow curvature parameters have been introduced, on the basis of experimental and numerical results from this thesis; these relationships are applicable for a wide range of hydraulic conditions;
- The inadequacies of some existing formulations of the sluice-gate flow have been quantified, and proper suggestions for improvement have been proposed;
- An update of the contraction distance and coefficient has been provided as an extension to the results from existing studies of the sluice flow problem;
- Detailed methods for computing two-phase turbulent flow passing underneath a sluice-gate using the Reynolds-averaged Navier-Stokes equations have been developed; the methods include strategies for computational model validations;
- This study has produced the valuable experimental data of sluice gate flow.

Chapter Two Literature Review

2.1 Classical studies of the sluice-gate problem

Consider the flow of water produced by a vertical sluice-gate in a horizontal channel of rectangular section (Figure 2-1). The flow is subcritical upstream from the gate and supercritical downstream from it. The supercritical outflow is a wall-bounded jet (Rajaratnam 1976), open to atmosphere (or free outflow). This outflow jet has a continuous profile $x_2 = f(x_1)$, with very high curvature at points on the free surface close to the gate. At a given point B on the free surface, the curvature is equal to the reciprocal of the radius, r, of the circle of curvature. The outflow possesses a vena contracta, where the flow area is minimum and cross-sectionally averaged velocity is at its maximum.

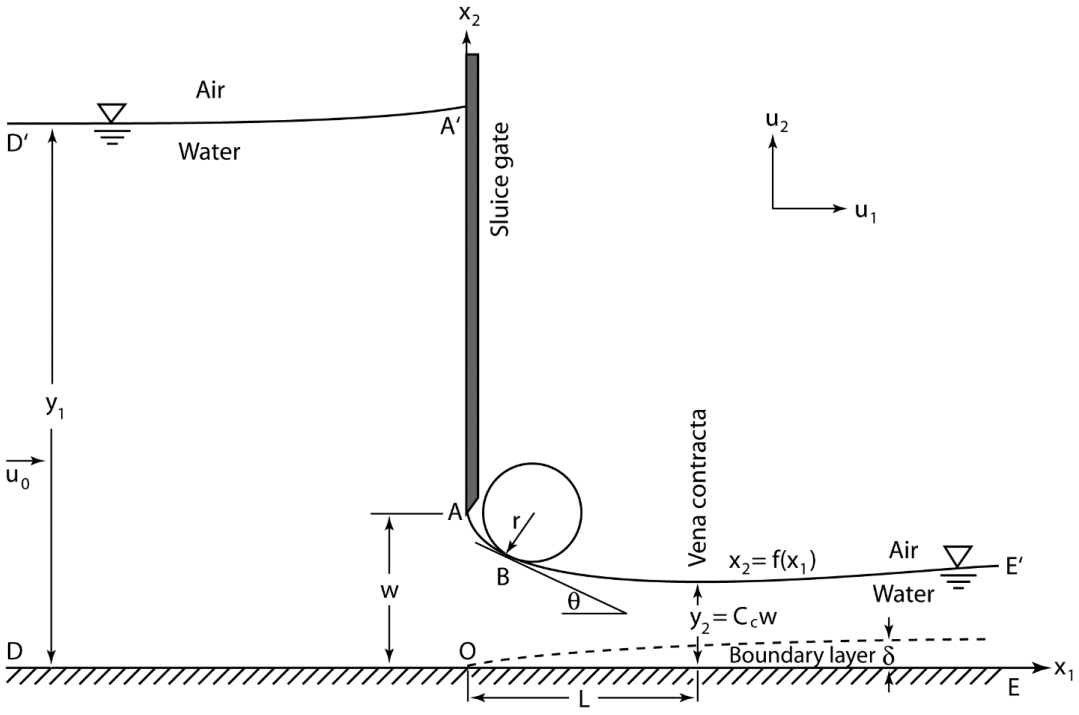

Figure 2-1: Definition diagram of flow passing underneath a vertical sluice gate. The gate is located at $x_1 = 0$, in a Cartesian coordinate system (x_1, x_2) with point O as its origin. Upstream from the gate, the approach flow has a velocity u_o in the x_1-direction and a depth y_1. Downstream

from the gate, a boundary layer develops along the bottom, with a thickness $\delta(x_1)$; at a given point B on the free surface, a tangent to the free surface makes an angle θ with the bottom.

Classical studies of sluice-gate flows have typically used a list of assumptions:

- The flow is steady, incompressible, and frictionless.
- The flow is one-dimensional, with straight streamlines and without turbulent velocity fluctuations.
- The flow is uniform at cross sections a short distance upstream as well as downstream of a sluice-gate.
- The associated pressure distribution in the flow is hydrostatic.

These assumptions substantially simplify the analysis of the flows, leading to analytical solutions without or with empirical coefficients.

When the approach flow (Figure 2-1) has a velocity head much smaller than the difference between the upstream depth y_1 and downstream depth y_2 (or $u_o^2/2g << y_1 - y_2$), the use of the energy equation yields an expression for the flow velocity, u_1, at the section of the vena contracta (or the y_2 section)

$$u_1 = \sqrt{2g(y_1 - y_2)} \qquad [2\text{-}1]$$

If the contraction coefficient, C_c, is known, one can calculate y_2 from the underflow gate opening w as $y_2 = C_c w$, calculate u_1 from Equation [2-1] for a given value of y_1, and further calculate the per unit width discharge q as

$$q = C_c w\sqrt{2g(y_1 - C_c w)} \qquad [2\text{-}2]$$

Equations [2-1] and [2-2] would underestimate the flow speed and discharge, due to the exclusion of the effect of $u_o^2/2g$ on q.

If the ratio y_1/w is not sufficiently large, Equations [2-1] and [2-2] become inadequate, because the assumption that the velocity head is negligible no longer holds. Without omitting the effect of the velocity head, the discharge is expressed as Henderson 1966:

$$q = C_d w\sqrt{2gy_1} \qquad [2\text{-}3]$$

where C_d is a discharge coefficient of the form $C_d = C_c/\sqrt{1 + C_c w/y_1}$. Values of C_c and hence C_d depend on the ratio y_o/w only. Note that the velocity head does not appear in Equation [2-3], but its effect has been included implicitly (Chow 1959). The results from the classical studies discussed above have not taken into account the effect of the non-uniform velocity distribution.

2.2 Experimental studies of the sluice-gate problem

Previously, many investigators have carried out laboratory experiments of sluice-gate flows for the purpose of determining the coefficients C_c and C_d. The results from well-referenced investigations show that the experimental values of C_c range from 0.59 to 0.75; C_c increases as the ratio y_1/w increases; C_c appears to show an asymptotic value of 0.61.

For instance, Lin et al. (2002) investigated the hydraulic jump in an open channel, by means of laboratory experiments. In the open-channel flume, the flow of water passed underneath a sluice gate, and a free flow hydraulic jump appeared on the downstream side of the sluice gate (Figure 2-2).

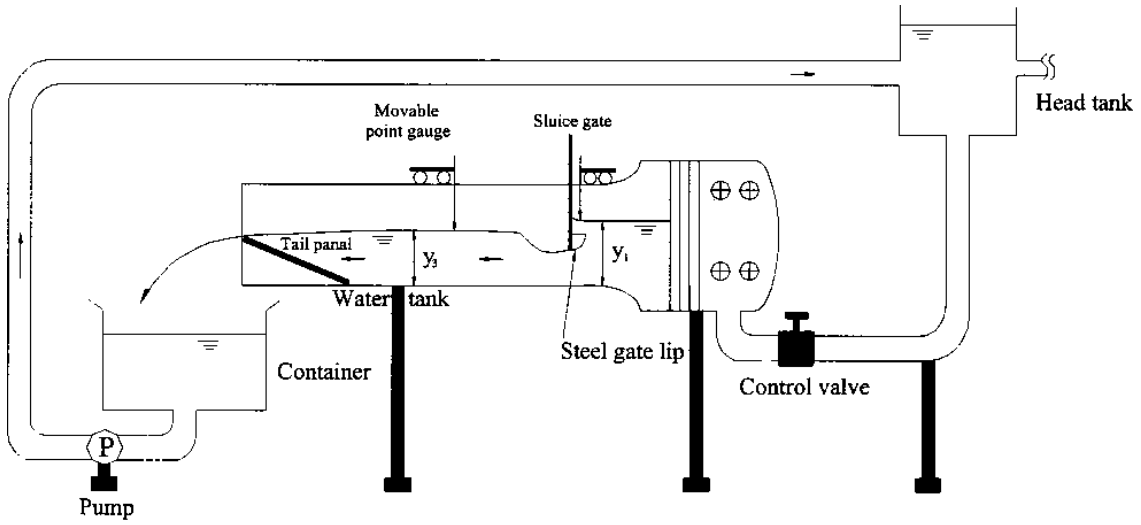

Figure 2-2: The layout of the equipment used in Lin et al. (2002) (from Lin et al. 2002).

The experiments showed a certain length of free flow before the hydraulic jump. Within this portion of free flow, the contraction coefficient, C_d, was measured. Lin et al. (2002) summarized the contraction coefficients measured in previous studies. For a vertical sluice gate, Henry (1950) reported $C_d = 0.60$, and Henderson (1966) determined $C_d = 0.61$. For tainter gates, Henderson (1966) suggested that C_d was in the range of 0.6 to 1.0. For planar sluice gates at different streamline angles, Montes (1997) reported that C_d ranged from 0.60 to 0.75. Other researchers point out that the contraction coefficient ranges from 0.65 to 0.75 for modified slide gates and from 0.59 to 0.61 for sharp-edged gates.

2.3 Numerical studies of the sluice-gate problem

Using available experimental data for comparisons, many researchers implemented different types of mathematical and numerical methods to predict details of the flow field for different regions of sluice gates. Mathematical models are useful for describing the flow phenomena.

For example, Montes (1997) used the inverse method to produce numerical solutions of the flow field. The author considered two-dimensional water flow passing underneath a sluice gate,

and used Laplace's equation to transfer the physical plane into the complex potential plane. In the calculations, the upstream flow was assumed to be inviscid and irrotational, and have constant specific energy (E).

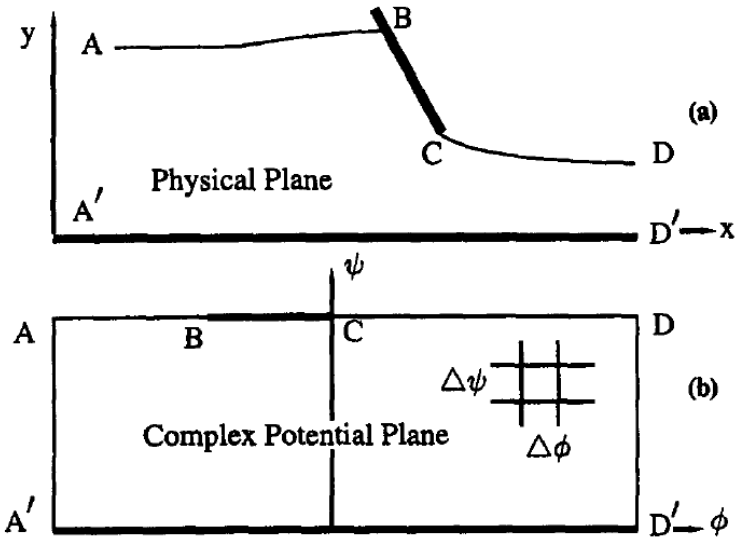

Figure 2-3: The transformation of the free flow phenomenon from the cartesian coordinates to the complex potential plane (from Montes 1997).

To reduce the artificial effects of model channel boundaries, Montes (1997) placed the inlet and outlet boundaries sufficiently far from the sluice gate. The author investigated the vertical sluice gate as well as inclined sluice gates at 45° and 60° from the horizontal direction. The main conclusion was that the assumption of inviscid and irrotational flow with constant specific energy (E) had very small effects on the results of contraction coefficient and pressure distributions on the gate surfaces, which agreed well with some reported experimental data (Montes 1997). Also, Montes (1997) concluded that with the consideration of gravity effect, calculated values for the contraction coefficient decrease with increasing ratio of the gate opening to specific energy (w/E). However, under the assumption of zero gravity, the trend is opposite.

The fast growth of computing power has made computer simulations of sluice-gate flow efficient and feasible to generate improved results. In a review of the previous studies, Kim (2007) suggested that mathematical models based on the potential flow theory could lead to persistent discrepancies of the contraction coefficient from experimental results. The experimental values of the contraction coefficient are usually 5 to 10% higher than the mathematical model results.

Kim (2007) solved the RANS equations using the finite volume method. The author established non-slip boundaries using the fractional area/volume obstacle representation method, and tracked the free surface using the VOF method. Kim (2007) treated non-slip walls by the wall function. The wall function considers the logarithmic layer in the near-wall region. The numerical simulations of Kim (2007) considered free surface geometry, real fluid flow and gravity. The results of Kim (2007) appear to show that the RANS equation model is effective to generate acceptable contraction and discharge coefficients.

Kim (2007) suggested that experimental values for the contraction coefficient were usually larger than the calculated values based on the potential flow theory. The numerical simulations of Kim (2007) gave larger contraction coefficients for smaller values for the ratio y_1/w. Experimental results show an opposite trend.

It is always desirable to achieve both high computational accuracy and efficiency. In this regard, the generation of good mesh for CFD computations is important. Akoz et al. (2009) performed a sensitivity test of the mesh setup in CFD computations using the finite element method. The authored used the VOF method (Nichols and Hirt 1975) to track the free surface, and two-equation models (the standard k-ε model and standard k-ω model) for turbulence closure.

Akoz et al. (2009) concluded that the VOF method was suitable for simulations of steady and unsteady free surface flows on fixed mesh.

For validations of the CFD models, the study of Akoz et al. (2009) included a series of laboratory experiments. The sensitivity test involved eight different mesh systems (Figure 2-4). The authored concluded that mesh refinements were very important for the regions of high-gradient changes of the velocity field and free surface profiles. Akoz et al. (2009) suggested that the standard k-ε model was more accurate and efficient than the standard k-ω model.

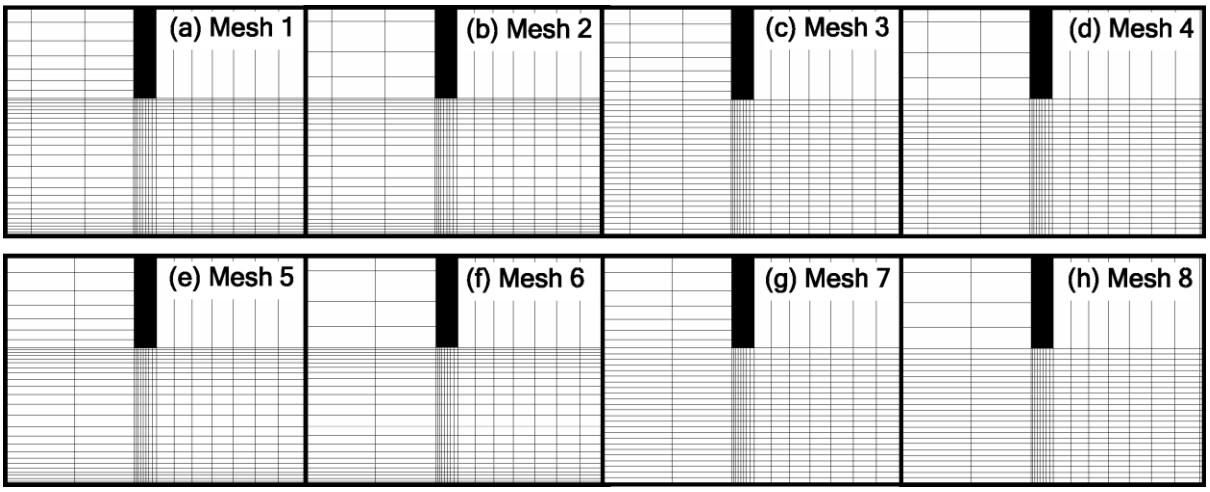

Figure 2-4: Eight types of mesh systems investigated in the study of Akoz et al. (2009) (from Akoz et al. 2009).

A summary of the contraction coefficients for free flow under a vertical sluice gate from previous experimental and numerical investigations is given in Table 2-1.

Table 2-1: The contraction coefficient of free flow under a vertical sluice gate.

Reference	y_1/w	C_c **(or** y_2/w**)**	**F** [a]
Experimental Investigation			
(Lin et al. 2002)	2–16	0.65–0.75	1.55-5.82
(Cheng et al. 1981)	2–10	0.59–0.61	1.28-6.72
(Akoz et al. 2009)	8.92	0.73	1.96
(Pajer 1937)	2.1–5	0.61	2.10-5.01
(Marchi 1953)	2.1	0.61	2.31
(Chung 1972)	>1.67	0.59–0.61	>2.00
(Roth and Hager 1999)	1.45–6.425	0.595	1.86-4.44
Numerical Investigation			
(Kim 2007)	1.67–10	0.618–0.63	1.96-5.52
(Khanpour et al. 2014)	9.167	0.71	4.90
(Montes 1997)	2-10	0.608–0.617	2.25-5.52

[a] The Froude number, F, is evaluated at the y_2 section.

Overall, the classical and many other existing studies of sluice-gate flows have been limited to the regions of uniform flow depth upstream from the y_1 section and downstream from the y_2 section (Figure 2-1). Between these two sections, the flow in the region close to the gate is rapidly varied flow; this is a problem to which solutions are far from being complete (Henderson, 1966). Among outstanding issues are the determination of realistic flow profiles from the gate opening to the section of the vena contracta, and the curvature of the flow. Knowledge of the varying curvature from the channel-bed to the curved free water surface is important. Existing studies resort to assumed curvature variations. This is an area of uncertainty.

Chapter Three Experimental Method

3.1 The flume system

Experiments of sluice-gate flow were performed using a laboratory flume in the Water Resources Engineering Laboratory at Concordia University (Figure 3-1). The flume channel is of rectangular cross section, with a constant width of 12.25 inches (or 31.115 cm). It has a length of 196 inches (or 497.84 cm). The channel-bed is made of stainless steel, and the sidewalls are made of tempered glass (Figure 3-2). Both the bed and sidewall surfaces are smooth. The channel-bed was set horizontal, with zero bed slope. The sluice-gate was installed vertically across the channel width at a longitudinal distance of 49.25 inches (or 125.095 cm) from the upstream end of the channel. The gate door has a bevelled lower edge.

Figure 3-1: Experimental Flume in Water Resources Engineering Laboratory at Concordia University, used in the study.

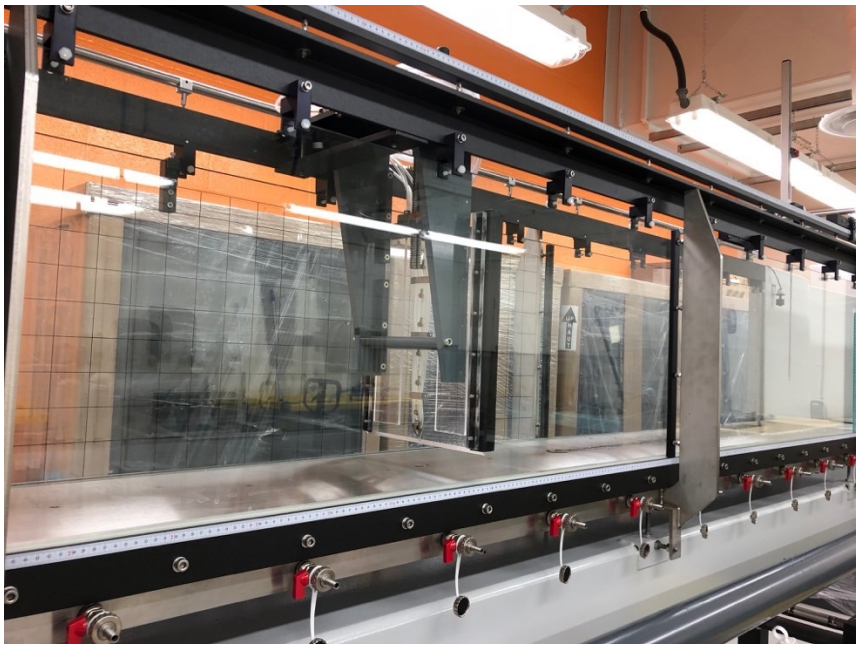

Figure 3-2: The channel-bed is made of stainless steel, and the sidewalls are made of tempered glass.

An inlet section made of stainless steel is fitted to the flume channel at its upstream end. This section has a length of 58.25 inches (or 147.995 cm), and a height matching that of the channel sidewalls. It has a constant width of 19.5 inches (49.53 cm) over its upstream two-thirds length, and then an S-curve tapering width that provides a match with the flume channel cross section. In the inlet section, there is a flat plastic board that floats at the free water surface during an experiment. An outlet section of 19.5 inches long (49.53 cm) is fitted to the flume channel at its downstream end. This outlet section has the same width and sidewall height as the flume channel. At the downstream end of this outlet section, a tilting weir is installed, which can be raised or lowered to produce a desirable flow depth in the flume channel during an experiment.

The flume channel, along with the inlet and outlet sections, is elevated 50.25 inches (or 127.635 cm) from the floor. A water supply reservoir (with a capacity of 2200 litres) on the floor is connected by a 3-inch inner-diameter pipe to the inlet section at the bottom. A 5-HP pump

(Lowara SHS4 model, manufactured by Xylem Inc., N.Y.) and an electromagnetic flowmeter (Promag 10D model, manufactured by Endress + Hauser Canada Ltd., Burlington, ON) are incorporated in the pipe. During an experiment, water is pumped from the reservoir up to the inlet section. Here, the S-curve contraction and floating board damp turbulent disturbances and help create uniform flow approaching the flume channel. Then, the flow of water passes through the sluice-gate opening and the outlet section and returns to the reservoir.

3.2 Experimental conditions

The experiments covered three different cases of the gate opening w: 1) w = 1 inch (or 2.54 cm); 2) w = 1.5 inches (or 3.81 cm); 3) w = 2 inches (or 5.08 cm), in combination of up to 13 different values for the ratio of flow depth, y_1, before the sluice-gate to gate opening. In the first case, experiments covered 13 different conditions of y_1/w = 4, 5,…, 16. In the second case, experiments covered seven different conditions of y_1/w = 4, 5,…, 10. In the third case, experiments covered five different conditions of y_1/w = 4, 5,…, 8. Thus, there is a total of 25 combinations of different w and y_1/w values. For each combination, experiments were repeated five times. In other words, a total of 125 experiments were performed in this study, as listed in Table 3-1.

It is understood that the dimensions of the flume channel and flow depth used are relatively small; therefore, it is necessary to access possible scale effects on the results if they are to be applied to field conditions. As will be explained in Sections 5.4 and 5.7, the scale effects have small impacts in the cases where w = 1 inch and 1.5 inches, but the results are acceptable. In the cases where w = 2 inches or larger, the experimental and numerical results are consistent. Therefore, the limitations of the experimental results are insignificant in this study.

Table 3-1: Summary of the hydraulic conditions for experiments of flow through sluice gate opening. The Froude number at the vena contracta is determined assuming a contraction coefficient of 0.62.

Parameter	**y1/w**	**Discharge Q (Litre per second)**	**Froude number F**	
			Before the gate	**At the vena contracta**
w = 2.54 cm	4,5,6,…,16	4.55 to 13.60	0.205 to 0.054	3.144 to 6.775
w = 3.81 cm	4,5,6,…,10	11.89 to 19.68	0.204 to 0.086	2.756 to 4.552
w = 5.08 cm	4,5,6,…,8	18.14 to 26.65	0.203 to 0.105	2.390

3.3 Measurements

Each of the 125 experiments produced measurements of: 1) flow depth before the sluice-gate, 2) profile of the free water surface (or flow curvature) after the sluice-gate, and 3) distributed pressures on the upstream face of the gate door at a series of depths below the free water surface (Figure 3-3). The depth of flow and the curved flow profile were measured using point gauges. These point gauges have an accuracy of 0.1 mm. The distributed pressures exerted on the gate door by the flowing water were made using manometers. These manometers have an accuracy of 1 mm. The pressure taps of the manometers were installed along the vertical centreline of the gate door, at vertical distances of 3.2, 9.6, 16.0, 28.7, 54.1, 104.9, 155.7, 206.5, 257.3 and 308.1 mm from the lower edge of the door.

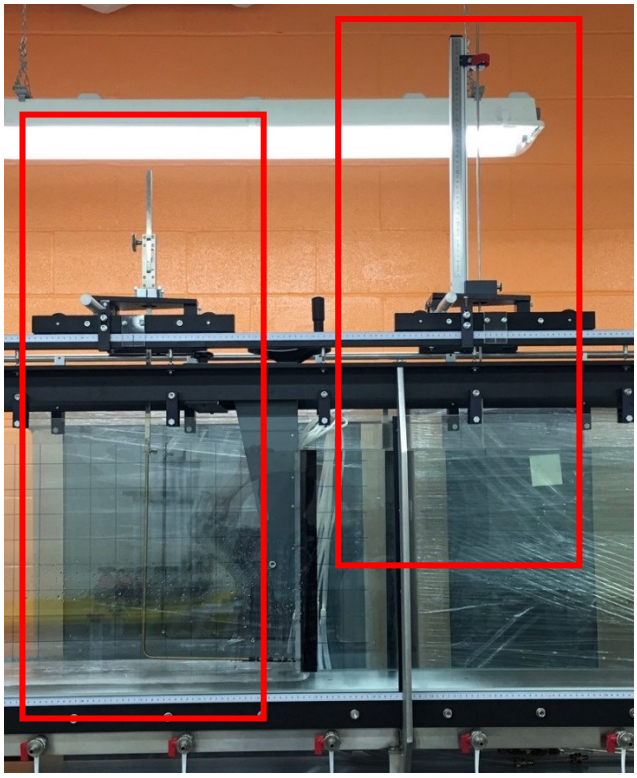

Figure 3-3: Measurer before the sluice gate (right hand side) to control the ratio of y_1/w; measurer after the sluice gate (left hand side) to measure the profile of flow on the downstream.

In addition, measurements of the discharge, Q, through the flume channel were obtained using an electromagnetic flowmeter. The measuring technique is based on Faraday's law of electromagnetic induction. The flowmeter is installed between the water pump and inlet section. It can measure flowrates from 0.044 to 45.278 L/s, at an accuracy of up to 0.028 L/s.

For each experiment, the Froude number is determined as $F = Q/(by_1^{3/2}g^{1/2})$ before the sluice-gate, and $F = Q/(0.62^{3/2}by_1^{3/2}g^{1/2})$ at the section of the vena contracta, where b is the width of the flume channel, and g is the gravity.

Chapter Four Numerical Model

4.1 Continuity and Momentum Equations for Two-phase Flow

Let ρ_a denote the density of air, ρ_w denote the density of water, μ_a denote the dynamic viscosity of air, and μ_w denote the dynamic viscosity of water and assuming that two-phase flow of water and air as a mixture is incompressible, the volume-weighted averages of the mixture density, ρ, and dynamic viscosity, μ, are:

$$\rho = \alpha_w \rho_w + (1 - \alpha_w)\rho_a \quad [4\text{-}1]$$

$$\mu = \alpha_w \mu_w + (1 - \alpha_w)\mu_a \quad [4\text{-}2]$$

where α_w is the volume fraction of water. For air, its volume fraction is $(1 - \alpha_w)$.

Let u denote the velocity vector of the mixture. In the Cartesian coordinate system, the continuity equation is expressed as:

$$\frac{\partial u_i}{\partial x_i} = 0 \quad [4\text{-}3]$$

The momentum equation is given by:

$$\frac{\partial \rho u_i}{\partial t} + \rho u_j \frac{\partial u_i}{\partial x_j} = -\frac{\partial p}{\partial x_i} + \mu \frac{\partial^2 u_i}{\partial {x_j}^2} + \rho g_i \quad [4\text{-}4]$$

where t is time; p is pressure; μ is dynamic viscosity.

Physically, the momentum equation [4-4] considers processes related to unsteadiness (the 1st term on the left-hand side), convection (the 2nd term on the left hand side), pressure gradient (the 1st term on the right hand side), diffusion (the 2nd term on the right hand side), and the combined effects of surface tension and gravity (the 3rd term on the right hand side). A more detailed description of these processes has been given in Akahori and Yoshikawa (2012).

4.2 Volume of Fluid Method for Tracking the Free Water Surface

One may track the position of the free water surface using the Volume of Fluid (VOF) method introduced by Hirt and Nichols (1981). Assuming that the gas and liquid phases are immiscible, in the absence of mass sources, the change of water volume fraction is governed by a convection equation of the form

$$\frac{\partial \alpha_w}{\partial t} + \nabla \cdot (\alpha_w u_i) + \nabla \cdot (\alpha_w (1 - \alpha_w) u_r) = 0 \qquad [4\text{-}5]$$

where u_r is surface internal energy density. Note that when α_w is equal to zero or one, the third term on the left-hand side of the above equation will be zero, which means the convection of fluids is pure. When α_w is between zero and one, the third term acts to compress the interface between two phases.

4.3 Reynolds-averaged Governing Equations

It is necessary to use the statistical approach since turbulent flows always contain fluctuations of different flow characteristics (Wilcox 2006, p. 34). This reason justifies the use of the averaging concept introduced by Reynolds (1895), where all flow variables can be expressed as a combination of mean and fluctuating parts. The averaging is applied to each of the terms in the continuity and Navier-Stokes equations.

4.3.1 Continuity and momentum equations of motion

The instantaneous dependent variables in Equation [4-3] and Equation [4-4] are individually decomposed into time-averaged and fluctuating quantities through Reynolds decomposition. The resultant Reynolds-averaged equations are time-averaged equations of motion for fluid mixture flow, given by

$$\frac{\partial \bar{u}_i}{\partial x_i} = 0 \quad [4\text{-}6]$$

$$\rho\left(\frac{\partial \bar{u}_i}{\partial t} + \bar{u}_j \frac{\partial \bar{u}_i}{\partial x_j}\right) = \rho g_i - \frac{\partial \bar{p}}{\partial x_i} + \mu \frac{\partial^2 \bar{u}_i}{\partial {x_j}^2} + \frac{\partial \tau_{ij}}{\partial x_j} \quad [4\text{-}7]$$

$$\frac{\partial \alpha_w}{\partial t} + \nabla \cdot (\alpha_w \bar{u}_i) + \nabla \cdot (\alpha_w (1 - \alpha_w) u_r) = 0 \quad [4\text{-}8]$$

where u_i is the velocity in x_i direction, t is time, ρ is fluid density, g_i is gravity, p is pressure, μ is dynamic viscosity, and τ_{ij} is the turbulent stress.

The Reynolds shear stress components in Equation [4-7] are the extra unknowns. In order to obtain numerical solutions to the governing equations on a mesh system, one needs to parameterise the Reynolds shear stress. In other words, one needs to use turbulence closure schemes. The schemes used in this paper are based on the Boussinesq approximation

$$\tau_{ij} = -\rho\overline{u_i' u_j'} = \mu_t \left(\frac{\partial \bar{u}_i}{\partial x_j} + \frac{\partial \bar{u}_j}{\partial x_i}\right) - \frac{2}{3}\rho k \delta_{ij}$$

[4-9]

where u_i' is velocity fluctuation in x_i direction, μ_t is turbulent viscosity, k is the turbulence kinetic energy, and δ_{ij} is Kronecker delta.

which relates the unknown shear stress to the mean flow strain rate through an eddy viscosity. In the following, two turbulence closure models are discussed. A comparison of their suitability will be given in Section 5.3 of this thesis.

4.3.2 The Standard k-ε Model

The standard k-ε model is a widely used two-equation turbulence closure model, and it is on the basis of the eddy-viscosity concept.

It belongs to the two-equation models. According to Launder and Spalding (1974), its governing equations of the turbulence parameters k (turbulence kinetic energy) and ε (dissipation rate) are:

$$\frac{\partial k}{\partial t} + u_j \frac{\partial k}{\partial x_j} = \frac{\partial}{\partial x_j}\left(\frac{\nu_T}{\sigma_k}\frac{\partial k}{\partial x_j}\right) + \nu_T\left(\frac{\partial u_i}{\partial x_j} + \frac{\partial u_j}{\partial x_i}\right)\frac{\partial u_i}{\partial x_j} - \varepsilon \qquad [4\text{-}10]$$

$$\frac{\partial \varepsilon}{\partial t} + u_j \frac{\partial \varepsilon}{\partial x_j} = \frac{\partial}{\partial x_j}\left(\frac{\nu_T}{\sigma_\varepsilon}\frac{\partial \varepsilon}{\partial x_j}\right) + C_1\frac{\varepsilon}{k}\nu_T\left(\frac{\partial u_i}{\partial x_j} + \frac{\partial u_j}{\partial x_i}\right)\frac{\partial u_i}{\partial x_j} - C_2\frac{\varepsilon^2}{k} \qquad [4\text{-}11]$$

where the distribution of eddy-viscosity ν_T gives:

$$\nu_T = C_\mu k^2/\varepsilon \qquad [4\text{-}12]$$

and C_1=1.44, C_2=1.92, C_μ=0.09, σ_k=1.0, σ_ε=1.3.

In this model, the transport equation for turbulence kinetic energy *k* (Equation [4-10]) determines the energy in the turbulence, and the transport equation for turbulence dissipation epsilon (Equation [4-11]) determines the rate of dissipation of the turbulence kinetic energy.

4.3.3 The SST k-ω Model

The shear stress transport (SST) k-ω model is another two-equation turbulence closure model. Menter (1994) introduced the model by combining the Wilcox k-ω model and the standard k-ε model. The k-ω formulation is used in the inner parts of the boundary layer (viscous sub-layer) to improve the simulation of flow behaviour in the viscous sub-layer. The SST k-ω model uses the following two transport equations

$$\frac{\partial k}{\partial t} + u_j \frac{\partial k}{\partial x_j} = P_k - \beta^* k\omega + \frac{\partial}{\partial x_j}\left[(\nu + \sigma_k \nu_T)\frac{\partial k}{\partial x_j}\right] \qquad [4\text{-}13]$$

$$\frac{\partial \omega}{\partial t} + u_j \frac{\partial \omega}{\partial x_j} = \alpha S^2 - \beta\omega^2 + \frac{\partial}{\partial x_j}\left[(\nu + \sigma_\omega \nu_T)\frac{\partial \omega}{\partial x_j}\right] + 2(1 - F_1)\sigma_{\omega 2}\frac{1}{\omega}\frac{\partial k}{\partial x_i}\frac{\partial \omega}{\partial x_i} \qquad [4\text{-}14]$$

Equation [4-13] gives the turbulence kinetic energy, and Equation [4-14] gives the specific turbulence dissipation rate. The turbulent eddy viscosity is calculated as

$$\nu_T = a_1 k / \max(a_1 \omega, SF_2) \quad [4\text{-}15]$$

where

$$F_2 = \tanh\left[\left[\max\left(\frac{2\sqrt{k}}{\beta^* \omega y}, \frac{500\nu}{y^2 \omega}\right)\right]^2\right] \quad [4\text{-}16]$$

$$P_k = \min\left(\tau_{ij} \frac{\partial u_i}{\partial x_j}\right) \quad [4\text{-}17]$$

$$F_1 = \tanh\left\{\left\{\min\left[\max\left(\frac{\sqrt{k}}{\beta^* \omega y}, \frac{500\nu}{y^2 \omega}\right), \frac{4\sigma_{\omega 2 k}}{D_{k\omega} y^2}\right]\right\}^4\right\} \quad [4\text{-}18]$$

$$D_{k\omega} = \max\left(2\rho\sigma_{\omega 2} \frac{1}{\omega} \frac{\partial k}{\partial x_i} \frac{\partial \omega}{\partial x_i}, 10^{-10}\right) \quad [4\text{-}19]$$

and $\alpha_1 = \frac{5}{9}$, $\alpha_2 = 0.44$, $\beta_1 = \frac{3}{40}$, $\beta_2 = 0.0828$, $\beta^* = 0.09$, $\sigma_{k1} = 0.85$, $\sigma_{k2} = 1$, $\sigma_{\omega 1} = 0.5$, $\sigma_{\omega 2} = 0.856$.

An advantage of the SST k-ω model is that it is less sensitive to the flow outside the boundary layer, because the closure switches to the k-ε model in the free-stream. The activation of using the k-ε model is achieved by introducing the blending function, F_1.

4.4 Boundary conditions

The model channel has five different types of boundaries: 1) water inlet, 2) air inlet, 3) solid walls, 4) outlet, and 5) atmospheric pressure at the top (Figure 4-1).

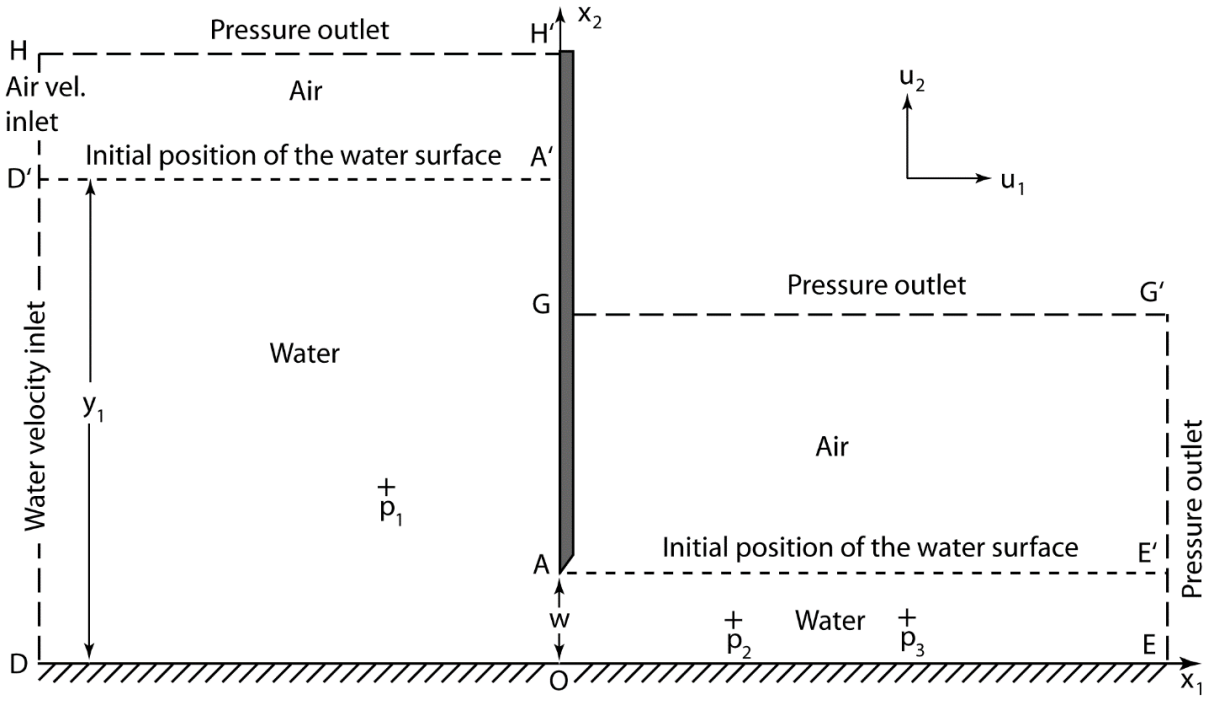

Figure 4-1: Model domain for numerical computations of flow passing underneath a sluice gate. Here, p1, p2, and p3 mark three selected locations for comparisons of numerical results among sensitivity test runs of the computational model.

At the water inlet, the horizontal velocity u_1 of water inflow is uniform in the vertical direction, which matches the experiment condition as

$$u_1 = Q/by_1 \qquad [4\text{-}20]$$

where u_1 the measured discharge, b is the flume width, and Q is the discharge. The vertical velocity of the inflow is

$$u_2 = 0 \qquad [4\text{-}21]$$

The turbulence kinetic energy k is calculated as

$$k = 3/2(Iu_1)^2 \qquad [4\text{-}22]$$

where I is the turbulence intensity (equals to 0.5%). The suitability of other values of turbulence intensity (3% and 12%) has been accessed. The results with I = 0.5% are the best, matching the experimental results. This is consistent with the findings from Dolinski et al. (2013).

At the air inlet, the inflow velocities

$$u_1 = u_2 = 0 \quad [4\text{-}23]$$

The water volume fraction is

$$\alpha_w = 0 \quad [4\text{-}24]$$

The turbulence kinetic energy is k has the same value as that at the water inlet.

At the outlet, u_1, u_2, k and α_w have zero gradient, without flow reversal.

At the atmospheric pressure at the top, u_1, u_2 and k have zero gradient, there is no water influx, and the water volume fraction is $\alpha_w = 0$.

Conditions at the solid walls are discussed below. The velocity component normal to the walls is zero, and the turbulence kinetic energy is given the same value as that at the water inlet.

The tangential component of velocity, and turbulence parameters ε, ω and ν_t are determined by wall functions. For a detail description, refer to Kalitzin et al. (2005) and Launder and Spalding (1974). The first node off a wall is in the logarithmic layer. The friction velocity u_τ is calculated from the k value at the node as

$$u_\tau = C_\mu^{1/4} k^{1/2} \quad [4\text{-}25]$$

where ν is the viscosity. The friction velocity is related to the wall shear stress τ_w as

$$u_\tau = \sqrt{\frac{\tau_w}{\rho}} \quad [4\text{-}26]$$

For the first node to fall inside the logarithmic layer, the wall distance, y^+, must be in the range of 30 to 200. The wall distance is defined as

$$y^+ = \frac{y u_\tau}{\nu} \quad [4\text{-}27]$$

where y is the distance to the wall, ρ is the density and μ is the dynamic viscosity.

The tangential velocity at the center of the first cell satisfies the following relationship:

$$u^+ = \frac{1}{\kappa}\ln(Ey^+) \quad [4\text{-}28]$$

where u^+ is defined in Equation [4-28], κ is the von Karman constant (equal to 0.41, and E is an empirical constant (equal to 9.8 for a smooth wall).

In dimensionless form, ε, ω, and ν_t are expressed as

$$\varepsilon^+ = \frac{1}{\kappa y^+} \quad [4\text{-}29]$$

$$\omega^+ = \frac{1}{\kappa\sqrt{C_\mu}y^+} \quad [4\text{-}30]$$

$$\nu_T = \nu \cdot \left(\frac{\kappa y^+}{\ln(Ey^+)} - 1\right) \quad [4\text{-}31]$$

In dimension form, the following wall functions are used to calculate ε, ω, u_1 as

$$\boldsymbol{\varepsilon^+ = \frac{\varepsilon\nu}{u_\tau{}^4}} \quad [4\text{-}32]$$

$$\omega^+ = \frac{\omega\nu}{u_\tau{}^2} \quad [4\text{-}33]$$

$$u^+ = \frac{u1}{u_\tau} \quad [4\text{-}34]$$

In the case of using the k-ε model, the ε value from Equation [4-20] enters Equation [4-10] for the calculation of k. In the case of the k-ω model, the w value from Equation [4-22] enters Equation [4-13] to calculate k.

4.5 Initial Conditions

At time t = 0, the flow velocities, u_1 and u_2, at all interior nodes are zero. The pressure distributions are hydrostatic.

When the k-ε model is used for turbulence closure, the initial conditions are as follows: At time t = 0, the initial values of the turbulence kinetic energy, k, and its dissipation rate, ε, are estimated on the basis of isotropic turbulence. They are given as

$$k = \frac{3}{2}(I|\boldsymbol{u_0}|)^2 \quad [4\text{-}35]$$

$$\varepsilon = \frac{C_\mu^{0.75} k^{1.5}}{L} \quad [4\text{-}36]$$

where I is the turbulence intensity, and $\boldsymbol{u_0}$ is the inlet velocity (or u_1 at $x_1 = -L_1$). In this study, I is assumed as 0.5%, and L is the reference length set to the inlet y_1. The turbulent eddy viscosity, ν_T, is calculated using Equation [4-12].

When the SST k-ω model is used for turbulence closure, the initial values of the turbulence kinetic energy and ε are also given by Equations [4-13] and [4-14]. In addition, the initial values of the turbulence specific dissipation, ω, is estimated by

$$\omega = \frac{k^{0.5}}{C_\mu L} \quad [4\text{-}37]$$

The initial values of the turbulent eddy viscosity, ν_T, area calculated using Equation [4-15].

For the standard k-ε model, at first, the software imports the initial values of k and ε, then reads the coefficients values as introduced in equations [4-10], [4-11], [4-12], [4-36], and [4-37]. Secondly, the turbulence viscosity is corrected for the whole field and boundaries by Equation [4-12]. Thirdly, the turbulence kinetic energy production term $\nu_T \left(\frac{\partial u_i}{\partial x_j} + \frac{\partial u_j}{\partial x_i}\right)\frac{\partial u_i}{\partial x_j}$ is calculated, and the correct production term is inputted in the boundary layer. Fourthly, the production term is put into equation [4-11] and calculate the new field of ε. Fifthly, the new ε and the production term is used in equation [4-10], and the new kinetic energy, k, is updated in the field and boundaries. Finally, since we have new values of k and ε, the second step is repeated to renew ν_T and the rest steps are repeated till the end.

For the standard SST k-ω model, the process is very similar to the standard k-ε model, except that the production term is $\frac{\partial}{\partial x_j}\left(\nu \frac{\partial k}{\partial x_j}\right)$, turbulence ν_T is calculated by equation [4-15],

viscosity k and ω are updated in the boundary layer by equations [4-13] and [4-14], and k and ε are updated in the field by using the blending function F_1 in equation [4-14].

4.6 Numerical Techniques

In this study, the finite volume method is used to solve the governing partial differential equations. This method has two advantages: First, it ensures the conservation of mass, the balance of momentum and energy at the discretized level. Fluxes are in balance between two adjacent controlled volumes. Second, its arbitrary meshing structures have excellent flexibilities to closely approximate the complex geometries (Kolditz, 2013).

At first, the model domain is discretized into a number of non-overlapping control volumes. Since the CFD model in this study is two-dimensional, each control volume is generally surrounded by four neighboring volumes in the field, or two ~ three neighboring volumes on the boundaries. Details can be found in Versteeg and Malalasekera (2007).

In the given two-dimensional situation, the distribution of property φ can be obtained by applying discretized equations at each grid node. On the boundaries, since the fluxes are known, the discretized equations are modified to incorporate boundary conditions.

In the governing partial differential equations [4-10], [4-11], [4-13], and [4-14], they have time terms and divergence terms on the left hand side, and the gradient terms and Laplacian terms on the right hand side. For each term, different mathematics schemes are used with the considerations of computational efficiency and accuracy.

For the time term (in the form of $\partial/\partial t$, such as $\frac{\partial k}{\partial t}$), the Euler scheme is chosen for it. Euler scheme is a bounded first order scheme designed for transient flows.

For the gradient terms (in the form of ∇, such as $\frac{\partial \bar{p}}{\partial x_i}$), Gauss Linear scheme is chosen as the scheme. The Gauss entry defines the standard finite volume discretization of Gaussian integration. In the integration process, the values are interpolated from cell centers to face centers. Following the Gauss entry, the Linear entry means the linear interpolation or central differencing. Gauss Linear scheme is a second-order scheme.

For the divergence terms (in the form of $\nabla \cdot$, such as $u_j \frac{\partial \omega}{\partial x_j}$, where u_j gives the advection flux), bounded Gauss upwind scheme is chosen for terms containing turbulence parameters and velocities, and other terms are assigned with Gauss linear. For bounded Gauss upwind, it means that the boundedness of the solution derived by the first order upwind scheme is maintained in order to provide a better convergence.

For the Laplacian terms (in the form of ∇^2, such as $\frac{\partial}{\partial x_j}\left(\frac{\nu_T}{\sigma_k}\frac{\partial k}{\partial x_j}\right)$), Gauss linear is chosen as the scheme for these terms.

In OpenFOAM, values of initial conditions and boundary conditions are assigned to the nodes of each controlled volume at first. Then the algorithm will assign a value at the center of each controlled volume based on the values on the surrounding nodes and boundary types, such as wall functions, fixed value, gradient formats, etc., in order to process the simulation by finite volume method. During the simulation, at each write interval (recording time point, not the time step), the simulated values for each used parameter will be re-assigned to the nodes of each controlled volume based on the boundary types and the value stored in the center of that controlled volume and written in corresponding files. Figure 4-2 explains the simulation process of OpenFOAM.

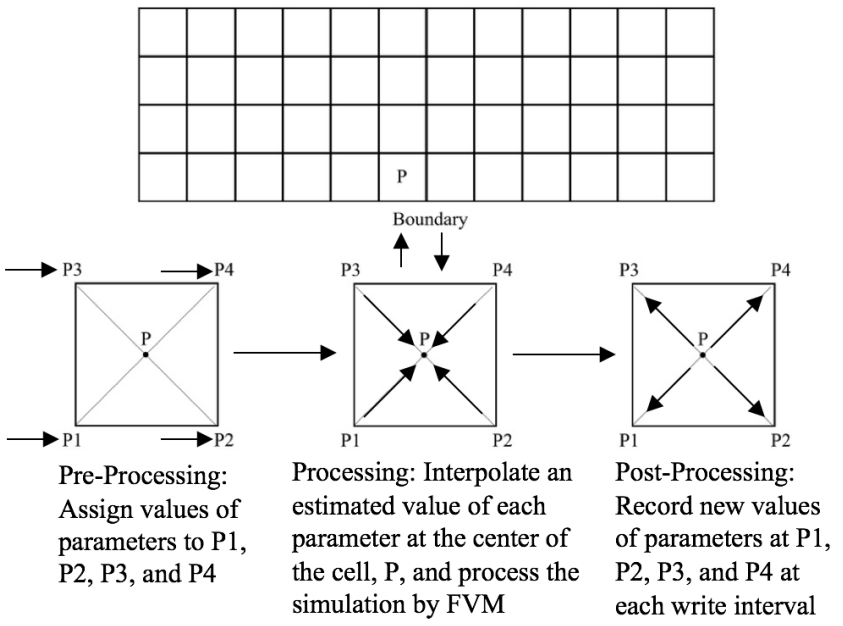

Figure 4-2: Simulation Process in OpenFOAM

In terms of the size of the first layer mesh close to the wall, the calculation is based on the flat-plate boundary layer theory explained by White and Corfield (2006):

$$\Delta s = \frac{y^+ \mu}{u_\tau \rho} \qquad [4\text{-}38]$$

where Δs is the spacing of the first layer mesh close to the wall. In this study, the spacing of the first layer mesh is chosen as 0.0001 m.

In addition, to achieve temporal accuracy and numerical stability, the Courant number should be less than 1 for every cell in the model. Given the definition of Courant number:

$$Co = \frac{\delta t |U|}{\delta x} \qquad [4\text{-}39]$$

where δt is the time step, $|U|$ is the velocity magnitude, and δx is the cell size. Since the minimal size of the cell is the spacing of the first layer mesh close to the wall, with the consideration of the free stream velocity in each situation, the time step, δt, is set as 0.0001s.

In OpenFOAM, most fluid dynamics solver applications use one of these three algorithms, namely PISO (pressure-implicit split-operator), SIMPLE (semi-implicit method for pressure-linked equations) and PIMPLE (combined PISO and PIMPLE). Equations of momentum and mass conservation are coupled by these algorithms. PISO and PIMPLE are used for transient problems, and SIMPLE is for steady-state. In this study, since the momentum equation (Equation [4-4]) contains a partial time term, $\frac{\partial \rho u}{\partial t}$, which means the model is transient; thus, the algorithm for pressure-velocity coupling is chosen as PIMPLE.

The simulations in this study allow a march of the transient flow to a steady state by retaining the unsteady term, $\frac{\partial \rho u}{\partial t}$, in the Navier-Stokes equations for better accuracy. The total CPU time of each simulation is about 2 hours, with parallel computations using 48 cores.

Chapter Five Results

5.1 Grid Convergence

Three test runs (MS1, MS2, and MS3 listed in Table 5-1) of the computational model were carried out for the purpose of determining mesh convergence of computational results. All the simulation conditions for these runs were the same, except the mesh size, δx. The mesh size was progressively refined from 0.2 to 0.1 to 0.05 cm (Table 5-1).

The computed Reynolds-averaged flow velocities (u_1, u_2) and water pressure p were extracted from the model results for three selected (x_1, x_2) locations, marked as p_1, p_2, and p_3 in Figure 4-1, at model time t = 20 s. The u_1, u_2 and p values are compared in Table 5-1. The comparisons show consistent values for the same (x_1, x_2) locations between MS2 and MS3. This confirms that grid convergence has been achieved. Thus, there is no need for further refinement of the mesh from Δx = 0.1 cm. This mesh size was used for subsequent model runs.

Table 5-1: Setup and conditions for test runs of the computational model, and comparisons of computed flow velocities (u1 and u2) and pressures (p) at selected locations (p1, p2, and p3, marked in Figure 4-1) among the test runs.

Run	Δt	Δx	Turbulence	w	y_1/w	u_o	p (Pa)	u_1 (m/s)	u_2 (m/s)	p (Pa)	u_1 (m/s)	u_2 (m/s)	p (Pa)	u_1 (m/s)	u_2 (m/s)
	(s)	(cm)	model	(cm)		(cm/s)	Location p_1			Location p_2			Location p_3		
MS1	0.0001	0.2	SST k-ω	5.08	8	21.018	3060.3	0.306	-0.234	69.7	2.712	-0.002	58.8	2.719	0.014
MS2	0.0001	0.1	SST k-ω	5.08	8	21.018	3061.1	0.307	-0.235	68.1	2.728	-0.003	59.3	2.724	0.007
MS3	0.0001	0.05	SST k-ω	5.08	8	21.018	3061.1	0.307	-0.235	68.1	2.728	-0.003	59.3	2.724	0.007
TS1	0.0001	0.1	SST k-ω	5.08	8	21.018	3061.1	0.307	-0.235	68.1	2.728	-0.003	59.3	2.724	0.007
TS2	0.00005	0.1	SST k-ω	5.08	8	21.018	3065.9	0.307	-0.234	67.6	2.729	-0.003	59.3	2.727	0.007
IC1	0.0001	0.1	SST k-ω	2.54	6	17.117	1047.6	0.205	-0.129	35.6	1.640	0.004	32.8	1.647	0.004
IC2	0.0001	0.1	SST k-ω	2.54	6	17.117	1055.1	0.205	-0.129	34.3	1.662	0.004	31.3	1.656	0.004
TC1	0.0001	0.1	SST k-ω	5.08	5	25.959	1563.7	0.276	-0.149	63.9	2.110	-0.002	59.3	2.108	0.006
TC2	0.0001	0.1	Standard k-ε	5.08	5	25.959	1483.4	0.278	0.102	103.7	1.795	0.011	103.4	1.819	0.010

5.2 Independence of model results on the choices of time step and initial conditions

Two test runs: TS1 and TS2 (Table 5-1), of the computational model were performed in order to confirm the independence of model results on the choice of time step. These two runs used the same simulation conditions, except the time step Δt. Here, Δt = 0.0001 s for TS1, and Δt = 0.00005 s for TS2. From the model results at model time t = 20 s, (u_1, u_2) and p were extracted for (x_1, x_2) locations p_1, p_2, and p_3 (Figure 4-1), compared in Table 5-1. It is shown that there are no significant differences of u_1, u_2 and p values at the same locations between TS1 and TS2. This confirms the independence of model results on the time step used. The time step of Δt = 0.0001 s is short enough to achieve numerical accuracy, and a further reduced Δt is not necessary.

The purposes of test runs IC1 and IC2 were to confirm the independence of model results on the choice of initial conditions. Initially, there was water of uniform depth [Figure 5-1(a)] equal to the gate opening downstream for IC1, whereas there was no water [Figure 5-1(b)] downstream from the sluice-gate for IC2. This was the only difference in simulation conditions between these two runs. In Table 5-1, IC1 and IC2 are shown to produce consistent results of flow velocity and pressure at selected locations at t = 20 s. Thus, the model results are independent of the initial conditions used. The initial condition shown in Figure 4-1 was used for all subsequent model runs.

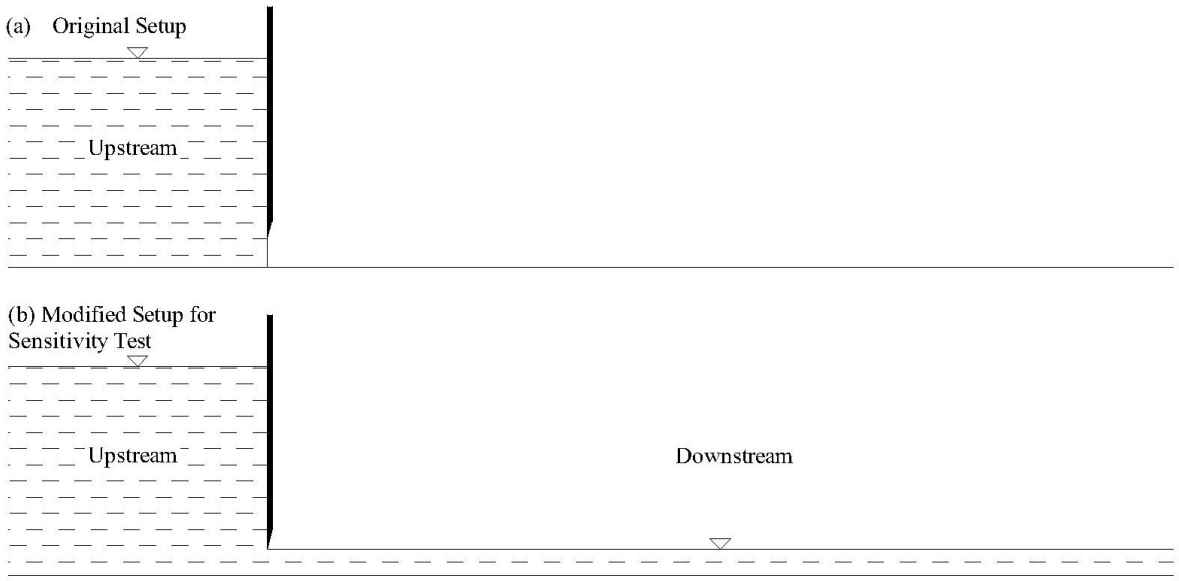

Figure 5-1: Sensitivity test of the choice of initial condition. a) the original setup for all of the simulations: the initial water position is placed before the sluice gate, with the desired flow depth, y_1, b) the modified setup for the sensitivity test: the initial water position is placed before and after the sluice gate. On the upstream, the flow depth is set as y_1; on the downstream, the flow depth equals to the gate opening size.

5.3 Suitability of turbulence closure schemes

The use of a proper turbulence closure scheme is important to computations of turbulent flow using the Reynolds-averaged approach. This section examines the suitability of two turbulence closure schemes: the SST k-ω model, and the standard k-ε model. The former was used in run TC1, whereas the latter was used in TC2 (Table 5-1). All other simulation conditions are the same between these two runs. In Figure 5-2, the computed flow profiles for TC1 and TC2 at model time t = 20 s are compared with measured flow profiles from the flume experiments, which are described in Section 2. Clearly, the prediction for TC1, which uses the SST k-ω model for turbulence closure, compares well with the experimental data. Run TC2, which uses the k-ε model for turbulence closure, has over-predicted the flow depth by about 15%. This finding is

consistent with Cassan and Belaud (2012) results. In this paper, subsequent model runs used the SST k-ω model for turbulence closure.

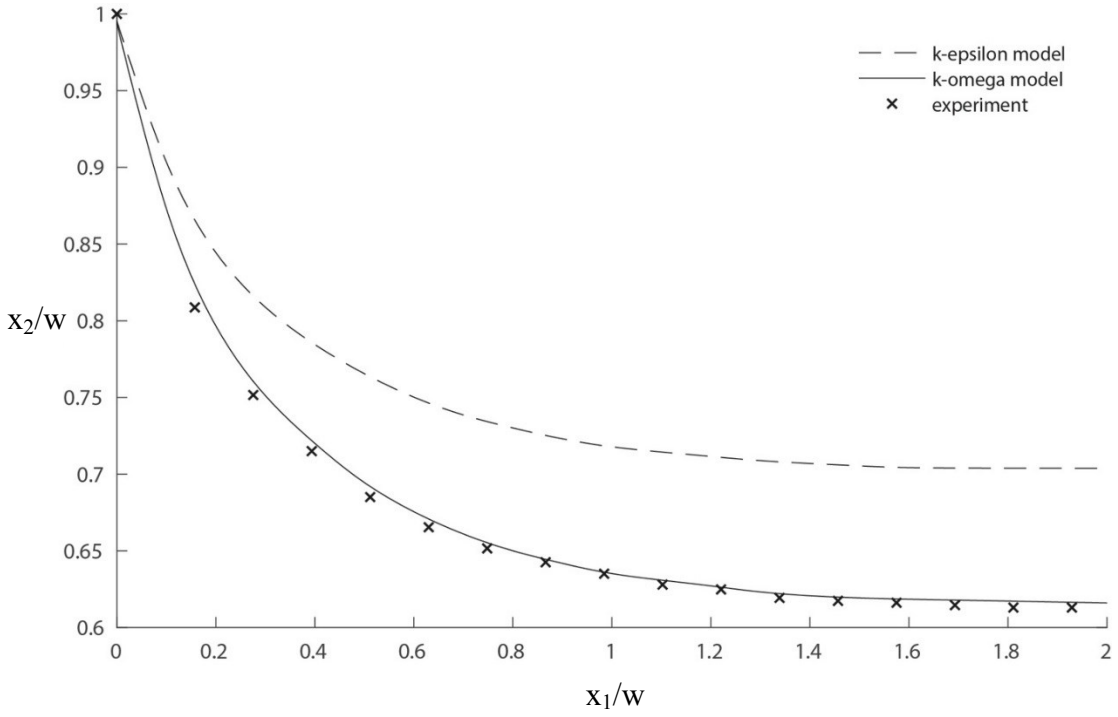

Figure 5-2: Comparisons of flow profiles downstream from the gate between runs (TC1 and TC2) and flume experiments, under matching hydraulic conditions. The gate opening is w = 5.08 cm. The upstream depth-to-gate opening is y_1/w = 5.

5.4 Validation of the computational model

This section gives validation of the computational model by comparing model predictions of flow variables with experimental data under a range of hydraulic conditions. The conditions cover the cases, where three different gate openings (or w = 2.54, 3.81 or 5.08 cm) are combined with five different upstream depth-to-opening ratios (or y_1/w = 4, 5,…, 8). It is understood that all the 15 individual combinations use the SST k-ω model for turbulence closure, a time step of Δt = 0.0001 s, and a simulation time period of T = 20 s.

In Figure 5-3(a)–(e), the computed flow profiles at model time t = 20 s for gate opening w = 2.54, 3.81, and 5.08 cm are plotted as the solid, long-dashed, and dot-dashed curves, respectively. The positions of the free water surface are determined using the criterion that the water volume fraction α_w = 0.5. The measured positions of the free water surface are plotted as the open triangle, circle, and square symbols. The curves are shown to plot through the symbols. This quantitatively confirms the quality of the model predictions. There are some minor discrepancies for the case of w = 2.54 cm. The computed curves are plotted slightly below the triangle symbols at relatively large longitudinal distances downstream from the gate opening. However, the discrepancies become insignificantly small at relatively large y_1/w ratios [Figure 5-3(d–e)]. Overall, the comparisons show that the computational model has produced acceptable results for the downstream side from the sluice-gate.

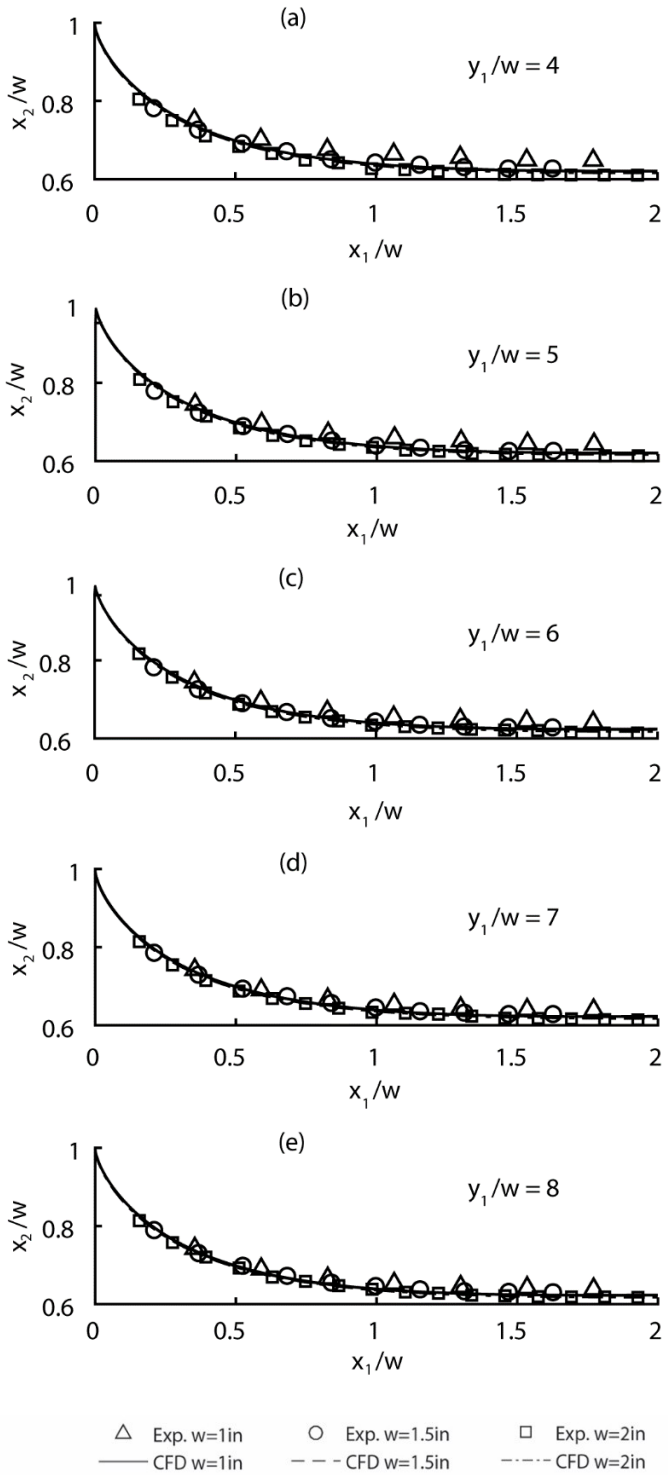

Figure 5-3: Longitudinal profiles of the water surface of flow after sluice gates, showing the surface curve for y_1/w equal to: (a) 4; (b) 5; (c) 6; (d) 7; (e) 8. The predicted flow profiles for w = 1, 1.5, and 2 inches are plotted as the solid, long-dashed, and short-dashed curves, respectively. The predictions are compared with the corresponding experimental data (the triangle, circle, and square symbols). The gate position is at $x = 0$ (the same hereafter).

It is constructive to further validate the model performance for the upstream side from the sluice-gate. For this purpose, vertical distributions of the computed pressures [Figure 5-4(a–c)] on the gate's upstream surface are compared with measured pressures from the experiments described in the "Experimental Method" section. In the figures, the vertical axis expresses the normalized vertical distance from the lower edge of the gate, given by

$$z = (x_2 - w)/(y_1 - w) \qquad [5\text{-}1]$$

and the horizontal axis represents the flow pressure normalized by the maximum value of $P(x_2)$ of the distributed pressure, given by

$$p' = p(x_2)/\max[p(x_2)] \qquad \text{for} \qquad w \le x_2 \le y_1 \text{ and } x_1 = 0 \qquad [5\text{-}2]$$

For 13 model runs, where w = 2.54 cm and y_1/w = 4, 5,…, 16, respectively, the computed p'-z curves virtually overlap, plotted as the solid curve in Figure 5-4(a). Corresponding measurements are plotted as the symbols. Clearly, the predictions agree well with the measurements. Similarly, good agreement is obtained for seven runs [Figure 5-4(b)], where w = 3.81 cm and y_1/w = 4, 5,…, 10, respectively, as well as for five runs [Figure 5-4(c)], where w = 5.08 cm and y_1/w = 4, 5,…, 8, respectively. Note that the maximum pressure occurs at z = 0.08 for w = 2.54 cm, and at z = 0.1 for w = 3.81 and 5.08 cm. The results show that at the lowest edge of the gate (or at z = 0), p' = 0.199, 0.179, and 0.107 for the three gate openings, respectively. The effects of the gate opening on the distributions of pressure on the gate are small. So are the effects of the ratio of the upstream depth to the gate opening. The favourable comparisons shown in Figure 5-2 and Figure 5-3 have confirmed the accuracy of the computational model.

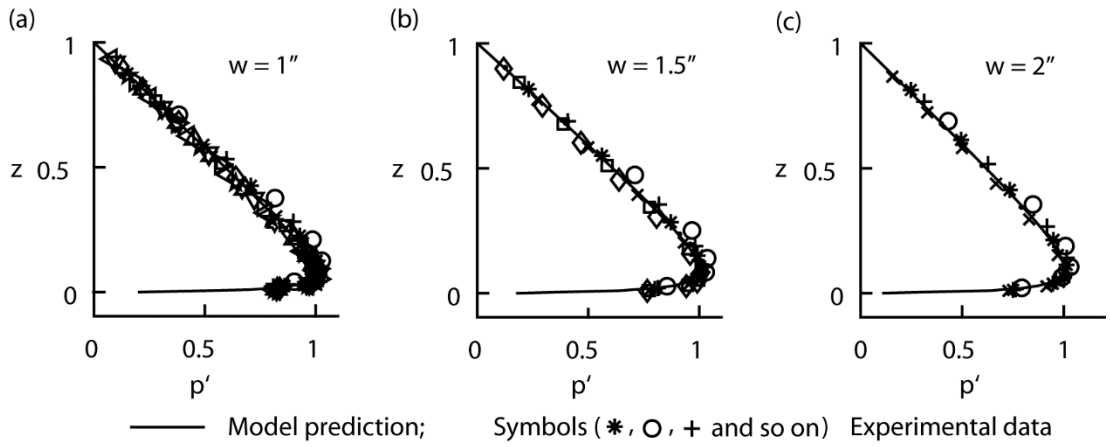

Figure 5-4: Distributions of pressure exerted on the gate door's upstream surface by water, with height above the door's lower edge (z = 0). The pressure has been normalised by the local hydrostatic pressure (Equation [5-2]). For y1/w = 4, 5, 6, …, 16, the normalised-pressure distributions predicted are virtually overlapped, their average being shown as the solid curve. Experimental data for the y_1/w values are plotted as symbols for comparison. The gate opening is equal to: (a) 1 inch (2.54 cm); (b) 1.5 inches (3.81 cm); (c) 2 inches (5.08 cm).

5.5 Curvature of flow profiles

The explicit function $x_2 = f(x_1)$ describes the free water surface. Some examples of which are shown as the solid curves in Figure 5-5. The curvature at a point (x_1, x_2) on the free water surface is (Zill et al., 2011):

$$\kappa = |f''| / (1 + f'^2)^{3/2} \qquad [5\text{-}3]$$

where f' and f'' denote the first and second derivative, respectively. At a given point, this paper evaluates f' and f'' with a fourth-order accuracy (Chung, 1972) as

$$f'(x_0) = [f(x_0-2\delta x) - 8f(x_0-\delta x) + 8f(x_0+\delta x)/3 - f(x_0+2\delta x)]/(12\delta x) + O(\delta x^4) \qquad [5\text{-}4]$$

$$f''(x_0) = [-f(x_0-2\delta x) - 16f(x_0-\delta x) - 30f(x_0) + 16f(x_0+\delta x) - f(x_0+2\delta x)]/(12\delta x^2) + O(\delta x^4) \qquad [5\text{-}5]$$

where x_0 is the coordinate of the point in the x_1-direction.

Modelling studies of two-phase flows have commonly used the criterion that the water volume fraction $\alpha_w = 0.5$ to track the free water surface. This can possibly result in some small waves on the free surface, as is the case shown in Figure 5-3. It is not important to analyse the

micro-scale (or local scale) curvature associated with these small spatial fluctuations. Thus, they are filtered out, yielding a smooth water surface (Figure 5-5) for the analysis of macro-scale curvature. The filtering process is based on a hyperbolic tangent model equation.

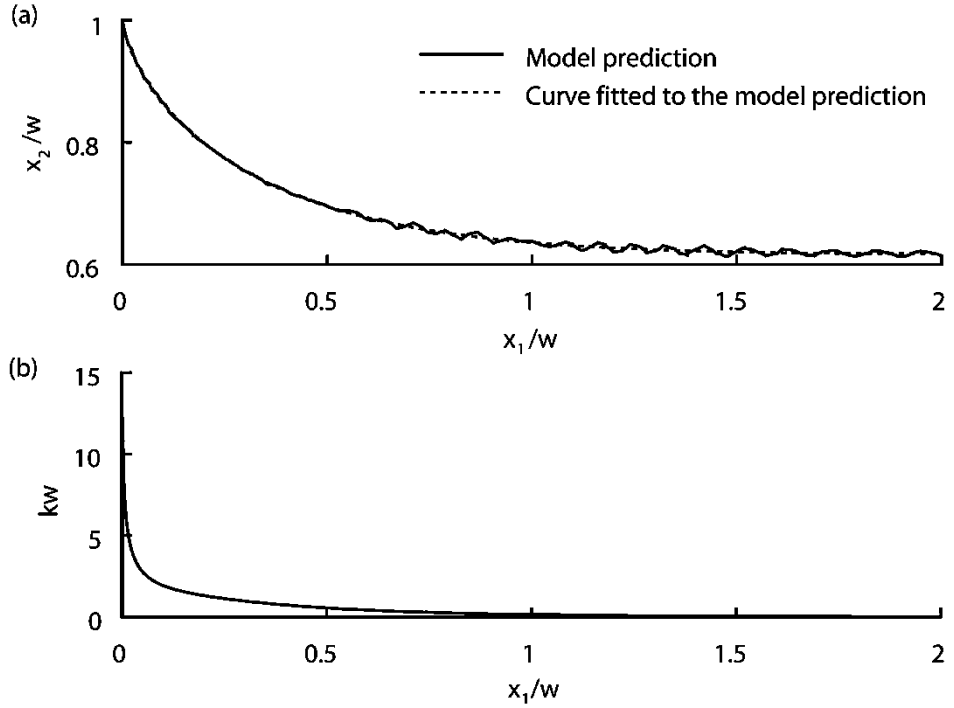

Figure 5-5: Predicted free water surface for TS1 (Table 5-1): (a) its positions as discerned on the basis of water volume fraction α_w = 0.5 directly from the model prediction, and hyperbolic tangent curve fitted to the predicted positions; (b) the curvature of the curve. The gate opening is w = 5.08 cm.

The curvature, κ, of the free water surface [Figure 5-5(a), the curve fitted to the model prediction] is determined using Equations [5-3]–[5-5]. The results of curvature in dimensionless form are plotted in Figure 5-5(b), which show that the curvatures decrease with increasing longitudinal distance downstream from the gate opening. The reciprocal of κ is known as the radius of the circle of curvature, denoted by r (Figure 2-1). For six selected points on the free

water surface, whose longitudinal coordinates are x_1/w = 0.0025, 0.25, 0.5, 0.75, 1.0, and 1.5, the circles (or part of them) of curvature and their centres are illustrated in Figure 5-6(a–g).

(x_{1c}, x_{2c}) denotes the centre of a circle of curvature in question. Fitting the results plotted in Figure 5-6(a–f) into non-linear polynomial functions yields the following empirical relationships for the curvature parameters:

$$r/w = a_r(x_1/w)^{b_r} + c_r(x_1/w) \quad [5\text{-}6]$$

$$(x_{1c}/w, x_{2c}/w) = [a_{1c}(x_1/w)^{b_{1c}} + c_{1c}(x_1/w),\ a_{2c}(x_1/w)^{b_{2c}} + c_{2c}(x_1/w)] \quad [5\text{-}7]$$

$$\theta = \pi/2 - a_\theta \tanh[b_\theta(x_1/w)^{c_\theta}] \quad [5\text{-}8]$$

The best fit was achieved with a_r = 3.486, b_r = 3.788, and c_r = 3.211; (a_{1c}, a_{2c}) = (0.618, 3.964), (b_{1c}, b_{2c}) = (0.316, 3.599), and (c_{1c}, c_{2c}) = (0.695, 2.36); a_θ = 1.712, b_θ = 1.374, and c_θ = 0.366.

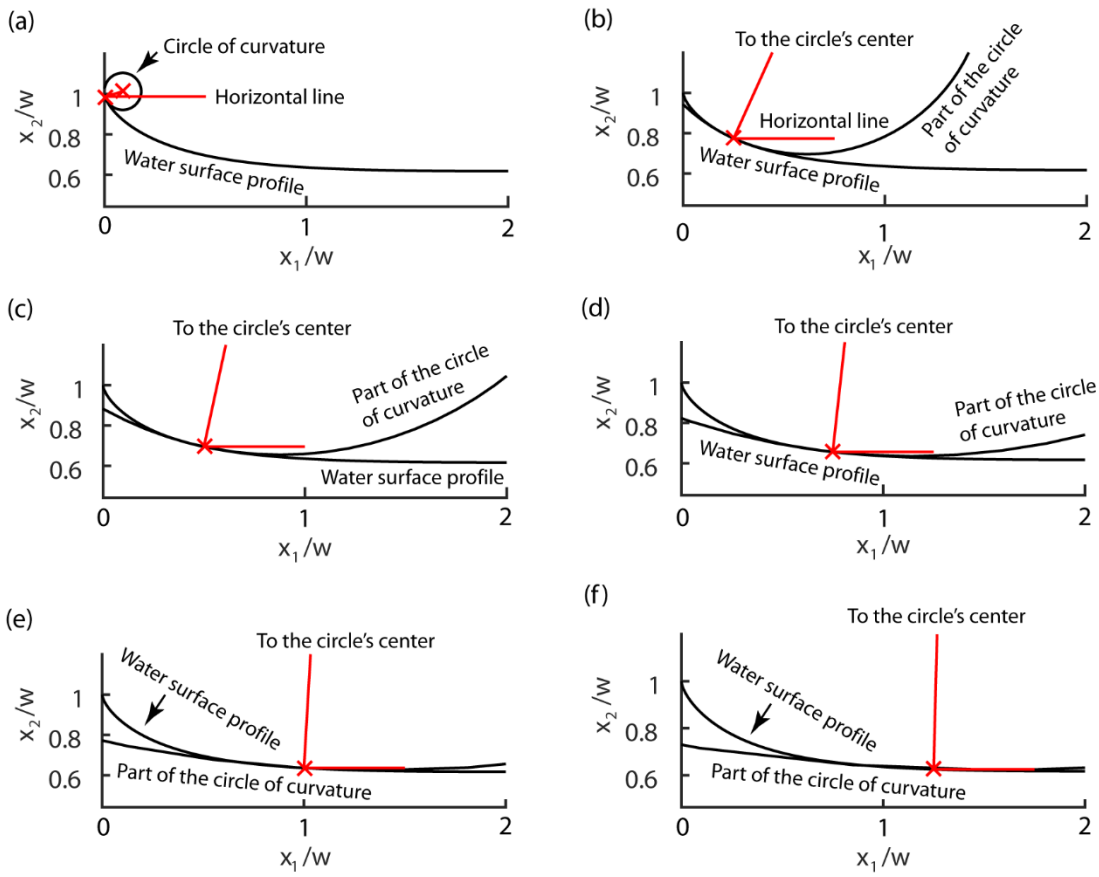

Figure 5-6: The circle (or part of the circle) of curvature and its center (or a line toward its center) at six selected points on the free surface. The results are for run TS1 (Table 5-1). The gate opening is w = 5.08 cm.

5.6 Contraction distance and contraction coefficient

For different sizes of sluice gate opening, Figure 5-3 shows that the smaller sluice gate can lead to a larger value of C_c. The details shown in Figure 5-7 also proves this observation. This observation also indicates that the scale effect is more significant for 1-in gate opening, but it is much smaller when gate opening is 1.5 inches or larger. Regarding the dimensionless contraction distance, where x_2/w on the downstream equals to C_c for the first time, the gate opening size has no significant influence on its value. As shown in Table 5-2, the dimensionless contraction distance just varies around the theoretical value, 1.5 (Henderson 1966).

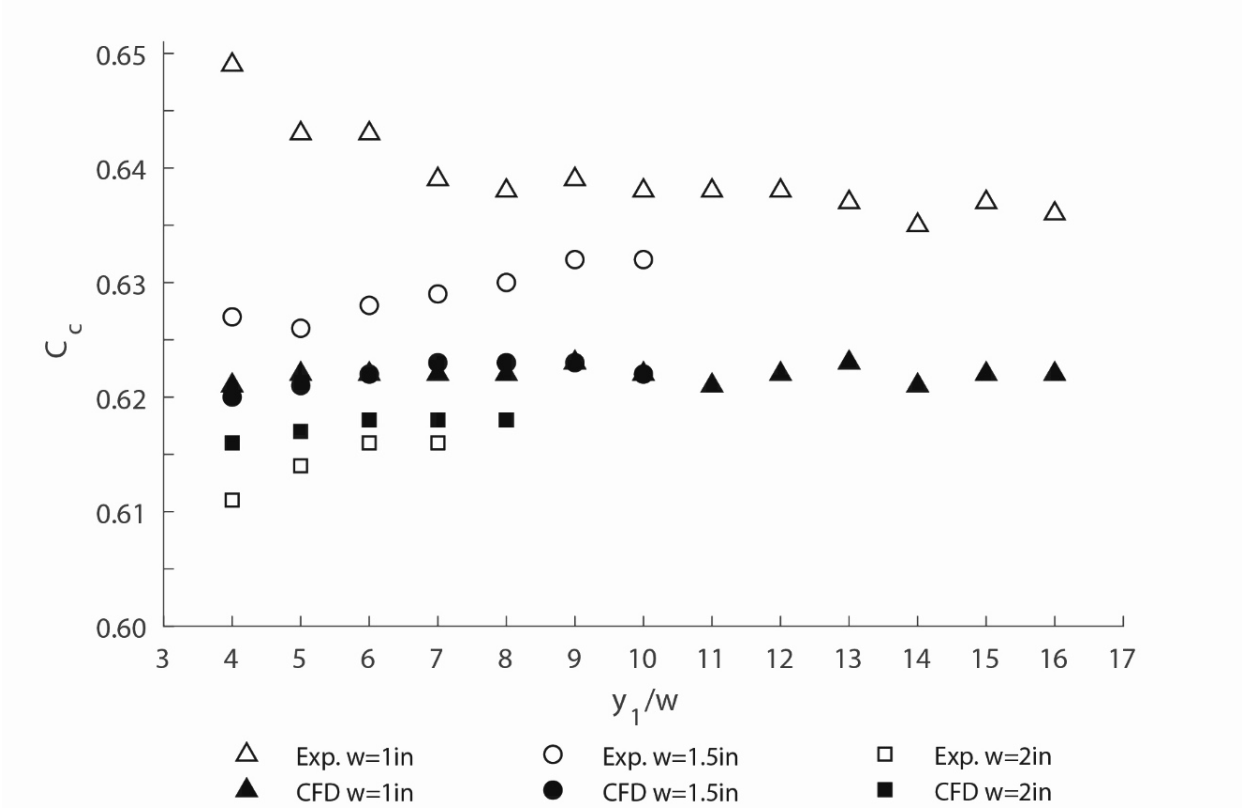

Figure 5-7: Values of the contraction coefficient, C_c, for y_1/w = 4, 5, 6,…, 16. The model predictions for w = 1, 1.5, and 2 inches are shown as the filled triangle, circle, and square symbols, respectively. The predictions are compared with the corresponding experimental data (the open triangle, circle, and square symbols).

As can be seen in Table 5-2, the results are: x_c/w = 1.772, 1.470, and 1.535 for w = 2.54, 3.81 and 5.08 cm, respectively. The corresponding estimates from the experimental data are: x_c/w = 1.575, 1.470, and 1.575. In this paper, x_c/w is considered as the contraction distance. The computational model appears to give over-prediction of the contraction distance at the small gate opening (w = 2.54 cm).

Table 5-2: Summary of Dimensionless Contraction Distance

Sluice Gate Opening Size, w (in)	Dimensionless Contraction Distance, x_c/w	
	Experimental Data	CFD Simulation
1	1.575	1.772
1.5	1.470	1.470
2	1.575	1.535

5.7 Curvature characteristics of flow passing underneath large gate opening

In order to reveal the applicability of the relations [5-6]–[5-8] to sluice-gate flows at scales closer to the prototype, three runs of the computational model at larger gate openings (w = 10.16, 20.32, and 40.64 cm) were carried out. For these three runs, $y_1/w = 6$. Analyses of the model results for the runs where w ranges from 5.08 to 40.64 cm give very consistent values for the coefficients in the relations. The mean values and standard deviations of the coefficients are: $a_r = 3.459 \pm 0.048$, $b_r = 3.812 \pm 0.018$, and $c_r = 3.196 \pm 0.011$; $(a_{1c}, a_{2c}) = (0.653 \pm 0.028, 3.948 \pm 0.043)$, $(b_{1c}, b_{2c}) = (0.308 \pm 0.009, 3.616 \pm 0.017)$, and $(c_{1c}, c_{2c}) = (0.711 \pm 0.022, 2.324 \pm 0.024)$; $a_\theta = 1.717 \pm 0.216$, $b_\theta = 1.359 \pm 0.010$, and $c_\theta = 0.364 \pm 0.002$. These standard deviations are less than 3% of the corresponding mean values for all the coefficients, expect (a_{1c}, a_{2c}), which are about 4%. Thus, the relevance of the relations [5-6]–[5-8] is confirmed.

5.8 The flow velocity field

In Figure 5-8, the distribution of water-velocity vectors for run TS1 (Table 5-1) is shown as an example to illustrate the structures of the flow field between the inlet (at $x_1/w = -6$) at upstream and $x_1/w = 3$ at downstream. At the inlet, the approach flow is in the horizontal direction, with a uniform speed. Above the gate opening, the horizontal velocity reduces in magnitude as the flow approaches the gate surface, the water flow nearby the flume bottom keeps their direction, but the velocity increases rapidly. With the increase of the height, the water flow starts to turn the

direction sooner or later. When the turning point gets closer to the sluice gate, the turning angle is larger. Especially for the water flow nearby the water surface, the flow streamline keeps horizontal till the sluice gate, and makes a 90° turn towards the gate opening.

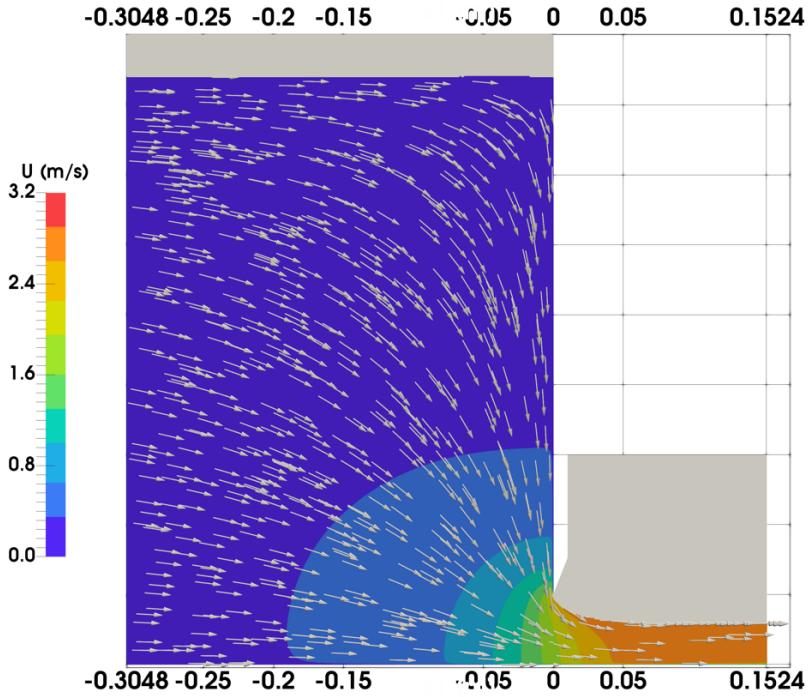

Figure 5-8: The flow velocity field. The scenario with 2-in gate opening and $y_1/w=8$. The investigated interval is from x_1/w = -6 to 3. Arrows represent the water flow directions in various points. Colours represent the flow velocity value.

For the structures of flow velocities after the gate, the water flow starts with various velocities and directions in different depths, and rapidly stabilizes into a horizontal flow with a uniform high velocity. When the flow is right below the sluice gate, the flow direction ranges from 0 to 90° from the flume bottom to the lower edge of the sluice gate. After that, the flow depth drops and stabilizes at a certain level. The flow velocity also increases to a high uniform value, and the flow direction becomes horizontal.

5.9 Distributions of turbulence intensity

In terms of the turbulence energy distribution, the relatively significant situation happens on the water flow after the sluice gate. As can be seen in Figure 5-9, when the water flow stabilizes with a certain height on the downstream, the turbulence energy reaches a peak value in the area nearby the flow surface. With the increase of the water depth, the turbulence energy decreases rapidly and reaches a uniform low value in the free flow zone. Special attention is drawn to the near wall region. In Figure 5-9, it is obvious that the turbulence energy is a little higher than the free flow zone in the region near the flume bottom.

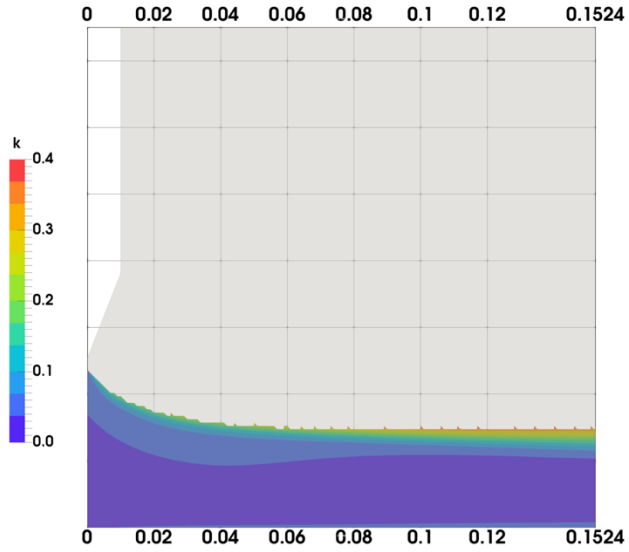

Figure 5-9: The turbulence energy distribution after the sluice gate in the scenario with 2-in gate opening and y1/w=8. The investigated interval, x1/w, ranges from 0 to 3.

5.10 Discussion

5.10.1 Division of highly curved flow profiles

Benjamin (1956) divided a sluice-gate flow into two parts by the section B (Figure 2-1) chosen as the section where the angle $\theta = 25°$, in order to simplify the analysis of the flow. The analysis was based on the assumption that downstream of B, the curvature, κ, of the free surface was insignificant. A correction of 5° needs to be made to the choice of the section B for the following reason. The angle θ equal to 25° occurs at a downstream distance (from the gate) of about one-fourth the gate opening (or at $x_1 \approx w/4$), as determined using Equation (23). At $x_1 = w/4$, κ remains the same order of magnitude as its maximum value immediately downstream from the gate, as calculated from Equation [5-3]. The curvature (Equation [5-3]) drops by an order of magnitude from the maximum value only after a downstream distance of about one-third the gate opening (or $x_1 \approx w/3$). At $x_1 = w/3$, the angle θ is equal to 20° (Equation [5-8]). Thus, a correction of 5° is proposed to Benjamin's (1956) assumption.

5.10.2 Non-hydrostatic pressure distribution

At a certain distance upstream from the gate or downstream from the gate, the distributions of pressure in the flow are expected to be hydrostatic. Rajaratnam and Humphries (1982) took this distance as five times the gate opening w, suggesting that the bottom pressure heads h_u at $x_1/w = -5$ and h_d and $x_1/w = 5$ had little deviations from the hydrostatic condition. From the computational results, this paper quantifies the deviations of bottom pressure head h_p in the near-gate region: $-3 \leq x_1/w \leq 3$, using the parameter given by

$$H_p = (h_p - h_d)/(h_u - h_d) \qquad [5\text{-}9]$$

where H_p values of unity and zero represent hydrostatic condition, respectively, for the regions upstream and downstream of the gate; values in between mean deviations from the condition.

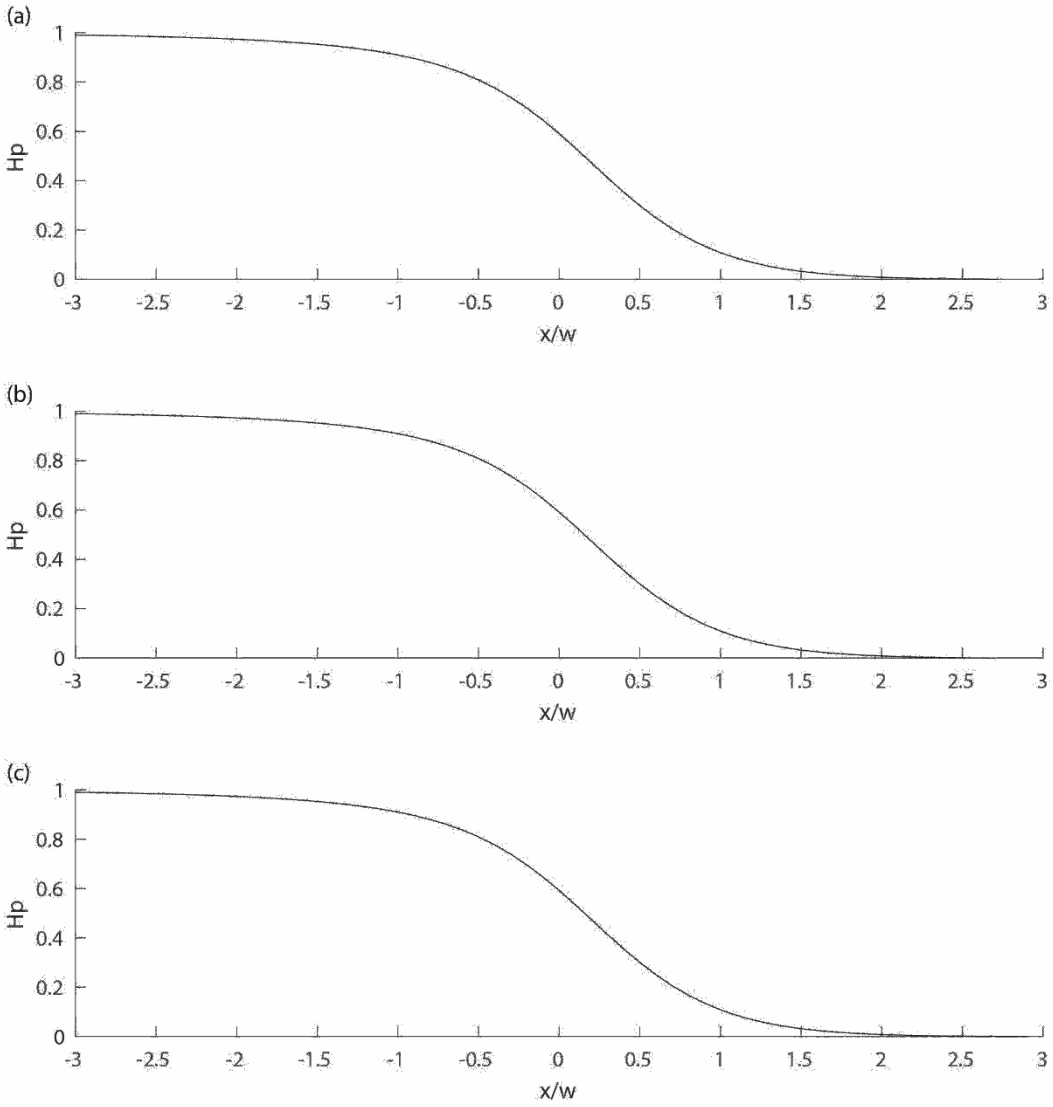

Figure 5-10: Longitudinal distributions of dimensionless pressure deviation (Equation [5-9]) on the channel-bed before and after sluice gates. For y_1/w = 4, 5, 6,…, 16, the dimensionless pressure-deviation distributions predicted are virtually overlapped, their average being shown as the solid curve. The gate opening is equal to: (a) 1 inch; (b) 1.5 inches; (c) 2 inches.

The profiles of H_p plotted in Figure 5-10 show large deviations in the vicinity of the gate. At the gate location (or $x_1 = 0$), for w = 2.54 cm, the (mean value ± standard deviation) of H_p are (0.59 ± 0.002) among runs where y_1/w = 4, 5,…, 16. Among runs where w = 3.81 cm, and y_1/w =

4, 5,…, 10, the mean value and standard deviation are (0.59 ± 0.003). This is also the case among runs where w = 5.08 cm and y_1/w = 4, 5,…, 8. The mean values of H_p are considerably different from unity and zero, meaning non-hydrostatic distribution. The deviations from hydrostatic condition are not negligible within an upstream or downstream (from the gate) distance equal to the gate opening. Therefore, the use of hydrostatic approximation should be cautioned against. This is regardless of the values for w and y_1/w. The profiles (Figure 5-10) indicate a 10% correction for non-hydrostatic pressure at $x_1 = \pm w$.

Table 5-3: Summary of the Bottom Pressure Immediately under the Sluice Gate

w = 1 inch						w = 1.5 inch			w = 2 inch		
h_1/w	Mean	Difference	h_1/w	Mean	Difference	h_1/w	Mean	Difference	h_1/w	Mean	Difference
4	0.59	0.005	10	0.59	0	4	0.591	0.005	4	0.592	0.005
5	0.59	0.003	11	0.59	0	5	0.591	0.003	5	0.592	0.001
6	0.59	0.001	12	0.59	0	6	0.591	-0.001	6	0.592	-0.002
7	0.59	0	13	0.59	-0.003	7	0.591	-0.001	7	0.592	-0.001
8	0.59	0	14	0.59	0.001	8	0.591	-0.002	8	0.592	-0.002
9	0.59	0	15	0.59	0.001	9	0.591	-0.002			
			16	0.59	0	10	0.591	-0.002			

5.10.3 Momentum and energy coefficients

The flow energy analysis that leads to the results given in Equations [2-1] – [2-2] has used the poor approximations that the flow is one-dimensional, and uniform at cross sections a short distance upstream and downstream of a sluice gate, and there are turbulent velocity fluctuations. More accurate results can be obtained by introducing the energy coefficient (Henderson 1966, p. 19), defined as $\alpha = \int u_1^3 dA\,/(u_{1m}^3 A)$, where A is the area of the cross-section in question, and u_{1m} is the cross-sectionally averaged velocity. This coefficient allows for the effect of variation in velocity at the cross section in question on energy flux. From the computed flow velocities, values for α are determined and plotted in Figure 5-11(a).

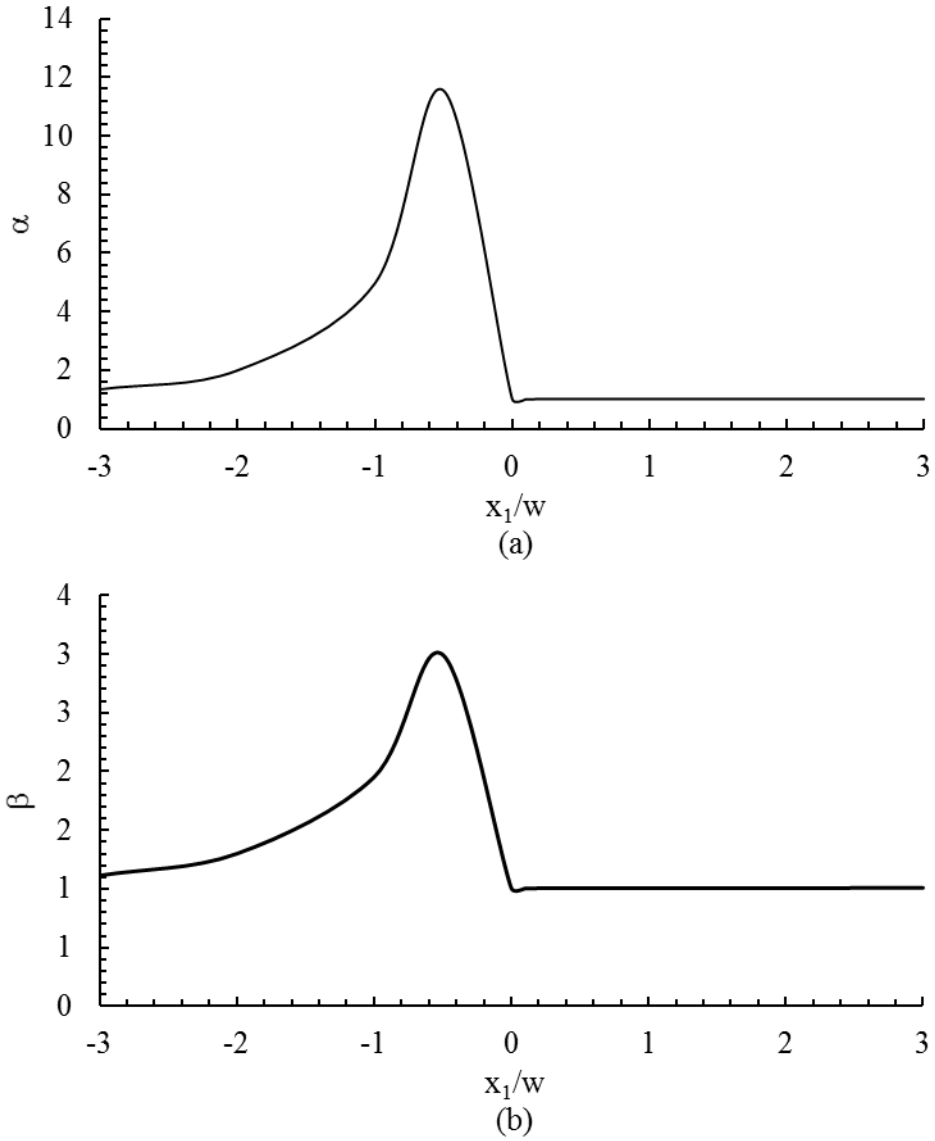

Figure 5-11: In the case where w = 2 inches and y_1/w = 6: (a) the variation of energy coefficient, α, with x_1/w from -3 to 3; (b) the variation of momentum coefficient, β, with x_1/w from -3 to 3.

Similarly, the momentum coefficient (Henderson 1966, p. 19), defined as, $\beta = \int u_1^2 dA \,/(u_{1m}^2 A)$, are also determined and shown in Figure 5-11(b). Introducing β to momentum analyses of the sluice-gate flow will improve the results.

5.10.4 The effect of gravity

Some previous studies (e.g. Benjamin 1956) of the sluice-gate flow problem have ignored the effect of gravity on the flow in order to simplify the analysis. Here, the differences of the computed free surface profiles [Figure 2-1, $x_2 = f(x_1)$] for five runs, where w = 5.08 cm and y_1/w = 4, 5,…, 8, with zero gravity (or g = 0), from the corresponding profiles, with g = 9.81 m/s^2, are quantified as

$$\Delta x_2 = (x_2|_{g=0} - x_2|_{g=9.81})/x_2|_{g=9.81} \qquad [5\text{-}10]$$

The results show that Δx_2 ranges from 12% (for y_1/w = 8) to 15% (for y_1/w = 4) at $x_1 = w$, and the percentages increase, respectively, to 14% and 16% at x_1 = 1.5w. This is to say that ignoring the effect of gravity leads to significant over-predictions of the flow depth after the sluice gate, and thus corrections are needed.

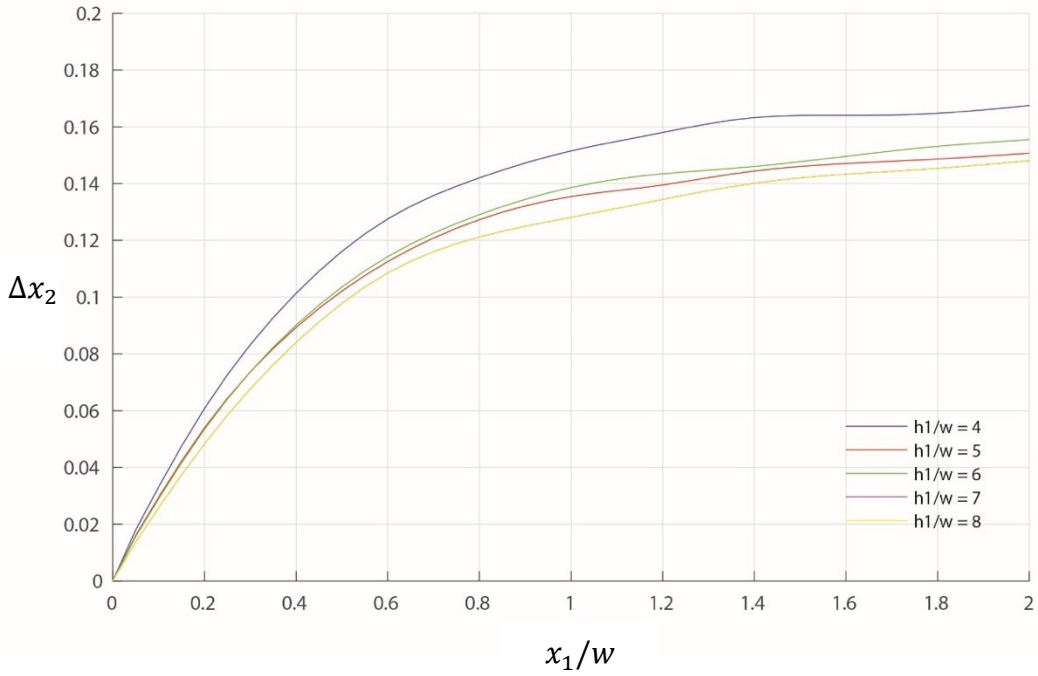

Figure 5-12: The relative difference in flow depth (Equation [5-10]) between predictions with gravitational effect and without, illustrating variation with longitudinal distance after sluice gates.

5.10.5 Thickness of bottom boundary layer

Discussions of the bottom boundary layer are given below for the region of $0 \leq x_1/w \leq 3$ for model runs where $y_1/w = 8$. According to Schlichting et al. (1955), the flow is laminar, when the Reynolds number, Re, is below the critical Reynolds number, $Re_{x\ crit}$

$$Re_{x\ crit} = \left(\frac{U_0 x_1}{\nu}\right)_{crit} = 5 \times 10^5 \qquad [5\text{-}11]$$

where U_0 is the freestream velocity, x_1 is the longitudinal distance from the sluice gate, and ν is the dynamic viscosity of water.

The bottom boundary layer thickness, δ, is defined as the distance normal to the bottom where the streamwise velocity is equal to $0.99U_o$. On the basis of the computational results for the model runs, the thickness is plotted in Figures 5.13(a–c) as the solid curves.

For the purpose of comparison, the thickness of a laminar boundary layer (Schlichting et al. 1955), given by

$$\delta = 5\sqrt{\frac{\nu x_1}{U_0}} \qquad [5\text{-}12]$$

is plotted in Figures 5.13(a–c) as the dashed curves. In the figures, the difference of free surface elevation between the model run where the bottom was a slip wall and the model run where the bottom a non-slip wall, are plotted as the dotted-dashed curves. The idea is to examine whether or not this difference is close to the boundary layer thickness obtained by the two methods explained above.

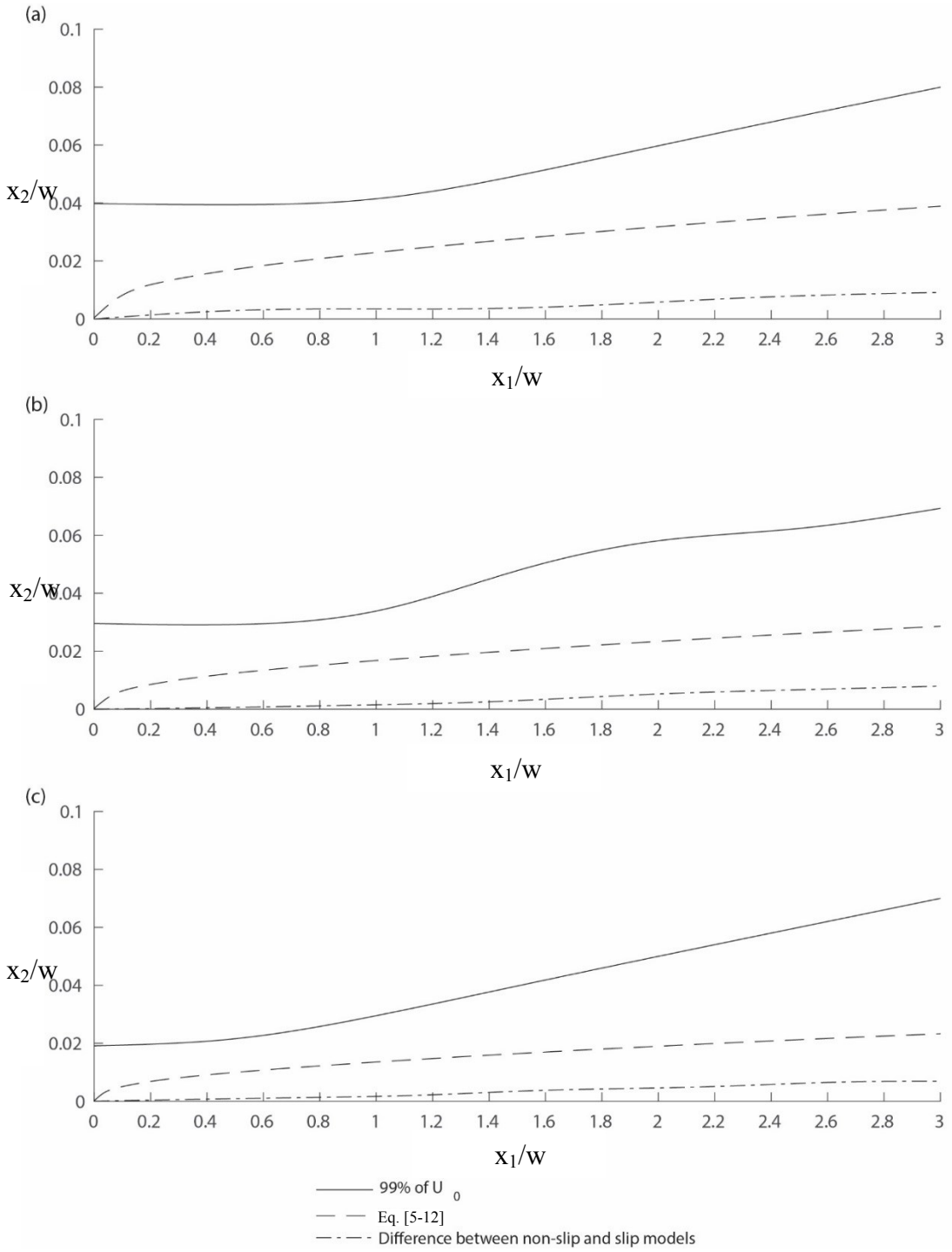

Figure 5-13: The bottom boundary layer after sluice gates for the gate opening equal to: (a) 2.54 cm; (b) 3.81 cm; (c) 5.08 cm.

The solid curves show larger boundary layer thickness for all three cases of the gate opening, which indicate that the boundary layer develops before the sluice gate. In particular, the thickness based on the definition of $0.99U_o$ is larger than that calculated by equation [5-12]. Regarding the difference of free surface elevations between slip and non-slip bottom runs, although the curves show a growing thickness in the flow direction, the thicknesses are small, compared to those based on the definition of $0.99U_o$. Thus, the difference does not reflect the true boundary layer thickness.

5.10.6 The effect of bottom friction

As expected, bottom friction has insignificant effect on the free surface profile [Figure 2-1, $x_2 = f(x_1)$] over the contraction distance. This is verified by comparing the computed free surface profiles for five runs, where w = 5.08 cm and y_1/w = 4, 5,…, 8, with a value of zero assigned to the kinematic viscosity of water (or $\nu = 0$), with the corresponding profiles, with $\nu = 1.05\times10^{-6}$ m^2/s. The relative differences are smaller than 1%. Thus, it would be acceptable to ignore the effect of bottom friction in simplified analyses of sluice-gate flow profiles, even at laboratory scale. Nevertheless, bottom friction is known to affect the transverse velocity gradient within the bottom boundary layer.

Chapter Six Conclusions

This paper reports new experimental and numerical results of turbulent flow passing underneath a sluice-gate. The focus is on the highly curved flow profiles downstream from the sluice-gate over the contraction distance, which have not received much research attention so far. The numerical results are obtained from solving the Reynolds-averaged continuity and momentum equations for two-phase flow of an air-water mixture. The following conclusions have been reached:

- The flow curvatures under a wide range of conditions (Table 3-1) in terms of the gate opening and upstream depth-to-gate opening ratio have been quantified from accurate and detailed point-gauge measurements, along with validated numerical results (Figure 2-1).
- For given conditions, the flow curvatures have a maximum value immediately downstream of the gate opening, and monotonically decay with increasing distance from the gate opening (Figure 5-5(b)).
- For the first time, reliable relationships (Equations [5-6] – [5-8]) for key flow-curvature parameters, namely the radius of the circle of curvature, the centre of the circle, and the angle of a tangent to the free surface with the channel-bottom, have been introduced. In dimensionless form, the lack of variations in these parameters under a wide range of conditions is remarkable. This represents a significant extension of the existing studies of the sluice-gate flow problem.
- The computed flow profiles as well as pressure distributions on the gate surfaces compare well with the experimental data (Figures 5-3 and 5-4). It is shown that the shear stress transport k-ω model provides suitable turbulence closure, and the volume of fluid method

is reliable for tracking the highly curved free surface. The computational methods have successfully been applied to produce results of flow passing underneath large gate openings (close to prototype scales).

- This thesis has provided an update of the contraction distance and coefficient to include large gate-opening flows (Table 5-2). The results are consistent with the literature values.
- The pressure distributions before and after the gate within a longitudinal distance equal to the gate opening show a significant deviation (Figure 5-10) from the hydrostatic distributions. In this connection, corrections are needed to the location for dividing flow profiles.
- The effect of gravity needs to be included in the analysis of the highly curved flow. The use of the momentum and energy coefficients from this paper would lead to an improvement in the results of future studies of the sluice gate flow problem using the momentum and energy principles.

For future work, the following four points should be further studied:

- The current research has dealt with vertical sluice gates. Future studies should consider other types of sluice gates such as Tainter gates, rolling gates and sluice gates with combined over- and underflow.
- This study covers the scenarios of free flow after the sluice gate. It would be interesting to conduct further research under conditions of submerged flow on the downstream.
- Future work should provide a comparison among different numerical approaches to simulating sluice gate flows.

- Finally, it would be interesting to systematically investigate the effects of turbulence on flow curvature.

References

Akahori, R., Yoshikawa, Y., and Yasuda, H. (2011). "Flexible control of density current migration by using sluice gate." *Journal of Japan Society of Civil Engineers. Ser. B*1*, Hydraulic engineering*, JSCE, **67**(40), 1585-1590.

Akoz, M.S., Kirkgoz, M.S., and Oner, A.A. (2009). "Experimental and numerical modeling of a sluice gate flow." *Journal of Hydraulic Research*, **47**(2), 167-176.

Baek, K.O., Ku, Y.H., and Kim, Y.D. (2015). "Attraction efficiency in natural-like fishways according to weir operation and bed change in Nakdong River, Korea." *Ecological Engineering-Elsevier*, **84**(11), 569-578.

Belaud, G., Cassan, L., Baume, J.P. (2009). "Calculation of contraction coefficient under sluice gates and application to discharge measurement." *Journal of Hydraulic Engineering-ASCE*, **135**(12), 1086-1091.

Benjamin, T.B. (1955). "On the flow in channels when rigid obstacles are placed in the stream." *Journal of Fluid Mechanics*, **1**(2), 227-248.

Cassan, L., and Belaud G. (2012). "Experimental and numerical investigation of flow under sluice gates." *Journal of Hydraulic Engineering-ASCE*, **138**(4), 367-373.

Cheng, A. H., Liu, P. L., and Liggett, J. A. (1981). "Boundary calculations of sluice and spillway flows." *Journal of the Hydraulics Engineering-ASCE*, **107**(10), 1163-1178.

Chern, M.J., and Syamsuri, S. (2013). "Effect of corrugated bed on hydraulic jump characteristic using SPH method." *Journal of the Hydraulics Engineering-ASCE*, **139**(2), 221-232.

Chow, V. T. (1959). *Open channel hydraulics.* McGraw-Hill Book Company, Inc., New York.

Chung, Y.K. (1972). "Solution of flow under sluice gate." *Journal of the Engineering Mechanics Division*-ASCE, 98(EM1), 121-140.

Finnie, J.I., and Jeppson, R.W. (1991). "Solving turbulent flows using finite elements." *Journal of Hydraulic Engineering-ASCE*, **117**(11), 1513-1530.

Habibzadeh, A., Vatankhah, A.R., and Rajaratnam, N. (2011). "Role of energy loss on discharge characteristics of sluice gates." *Journal of Hydraulic Engineering-ASCE*, **137**(9), 1079-1084.

Henderson, F.M. (1966). *Open Channel Flow*, Macmillan, New York.

Hirt, C.W., and Nichols, B.D. (1981). "Volume of fluid (VOF) method for the dynamics of free boundaries." *Journal of Computational Physics-Elsevier*, **39**(1), 201-115.

Kalitzin, G., Medic, G., Iaccarino, G., and Durbin, P. (2004). “Near-wall behavior of RANS turbulence models and implications for wall functions.” *Journal of Computational Physics-Elsevier*, **204**(1), 265-291.

Khanpour, M., Zarrati, A.R., and Kolahdoozan, M. (2014). “Numerical simulation of the flow under sluice gates by SPH model.” *Transactions A: Civil* Engineering-Scientia Iranica, **21**(5), 1503-1514.

Kim, D.G. (2007). “Numerical analysis of free flow past a sluice gate.” *Journal of Civil Engineering-KSCE*, **11**(2), 127-132.

Kolditz, O. (2013). *Computational methods in environmental fluid mechanics*. Springer Science & Business Media, Berlin, Germany.

Launder, B.E., and Spalding, D.B. (1974). “The numerical computation of turbulent flows.” *Computer Methods in Applied Mechanics and Engineering-Elsevier*, **3**(2), 269-289.

Lin, C.H., Yen, J.F., and Tsai, C.T. (2002). “Influence of sluice gate contraction coefficient on distinguishing condition.” *Journal of Irrigation and Drainage Engineering-ASCE*, **128**(4), 249-252.

Marchi, E. (1953). "Sui fenomeni di efflusso piano da luci a battente." *Annali Di Matematica Pura Ed Applicata,* **35**(1), 327-341.

Masliyah, J.H., Nandakumar, K., Hemphill, F. and Fung, L. (1985). “Body-fitted coordinates for flow under sluice gates.” *Journal of Hydraulic Engineering-ASCE*, **111**(6), 922-933.

Menter, F. R. (1994). "Two-equation eddy-viscosity turbulence models for engineering applications." *AIAA Journal-AIAA*, **32**(8), 1598-1605.

Montes, J. (1997). "Irrotational flow and real fluid effects under planar sluice gates." *Journal Hydraulic Engineering-ASCE,* **123**(3), 219-232.

Moreno, M., Maia, R., and Couto, L. (2016). “Prediction of equilibrium local scour depth at complex bridge piers.” *Journal of Hydraulic Engineering-ASCE*, **142**(11), 04016045-1-04016045-13

Pajer, G. (1937). "Über den Strömungsvorgang an einer unterströmten scharfkantigen Planschütze." *Journal of Applied Mathematics and Mechanics/Zeitschrift Für Angewandte Mathematik Und Mechanik-ZAMM,* **17**(5), 259-269.

Rajaratnam, N. (1976). *Turbulent jets. Vol. 5.*, Elsevier Scientific, New York.

Rajaratnam, N., and Humphries, J. (1982). "Free flow upstream of vertical sluice gates." *Journal of Hydraulic Research-Taylor and Francis*, **20**(5), 427-437.

Reynolds O. (1895). “On the dynamical theory of incompressible viscous fluids and the determination of the criterion.” *Philosophical Transactions A-The Royal Society*, **186**(1), 123–164.

Roth, A., and Hager, W.H. (1998). “Underflow of standard sluice gate.” *Experiments in Fluids-Springer*, **27**(4), 339-350.

Schlichting, H. (1955). *Boundary-layer theory*, McGraw-Hill, New York.

Shammaa, Y., Zhu, D.Z., and Rajaratnam, N. (2005). “Flow upstream of orifices and sluice gates.” *Journal of Hydraulic Engineering-ASCE*, **131**(2), 127-133.

Termini, D. (2009). “Experimental observations of flow and bed processes in large-amplitude meandering flume.” *Journal of Hydraulic Engineering-ASCE*, **135**(7), 575-587.

Versteeg, H.K., and Malalasekera, W. (2007). *An introduction to computational fluid dynamics*, Pearson, Essex, UK.

Wang, H.Z., Liu, X.Q., and Wang, H.J. (2016). “The Yangtze river floodplain: threats and rehabilitation.” *American Fisheries Society Symposium-AFS*, **84**(1), 263-291.

White, M. (2006). *Viscous Fluid Flow*, McGraw-Hill, New York.

Wilcox, D.C. (2006). *Turbulence modeling for CFD*, DCW, La Canada, California

Xie, C., and Lim, S.Y. (2015). "Effects of jet flipping on local scour downstream of a sluice gate." *Journal of Hydraulic Engineering-ASCE*, **141**(4), 04014088-1- 04014088-23

Zhang, J., Jørgensen, S. E., Tan, C. O., and Beklioglu, M. (2003). "A structurally dynamic modelling—Lake Mogan, Turkey as a case study." *Ecological Modelling-Elsevier*, **164**(2), 103-120.

Zhang, S.Y., Duan, J.G., and Strelkoff, T.S. (2013). "Grain-scale nonequilibrium sediment-transport model for unsteady flow." *Journal of Hydraulic Engineering-ASCE*, **139**(1), 22-36.

Zhang, W., Liu, M., Zhu, D.Z., and Rajaratnam, N. (2014). "Mean and turbulent bubble velocities in free hydraulic jumps for small to intermediate Froude numbers." *Journal of Hydraulic Engineering-ASCE*, **140**(11), 04014055-1- 04014055-9.

Zill, D., Wright, W. S., and Cullen, M. R. (2011). *Advanced engineering mathematics*, Jones & Bartlett Learning, Burlington, Massachusetts

Zimmer, A., Schmidt, A., Ostfeld, A., and Minsker, B. (2013). "New method for the offline solution of pressurized and supercritical flows." *Journal of Hydraulic Engineering-ASCE*, **139**(9), 935-948.